Available online at www.sciencedirect.com
ScienceDirect
Trans. Nonferrous Met. Soc. China 35(2025) 2105−2134
Transactions of Nonferrous Metals Society of China
www.tnmsc.cn

Phase prediction and mechanical responses of high-entropy alloys

Bin LI[1], Jia-lin SUN[1,2,3], Jun ZHAO[4], Xia-lun YUN[5], Quan-bin DU[6]

1. School of Mechanical, Electrical & Information Engineering, Shandong University, Weihai 264209, China;
2. Shenzhen Research Institute of Shandong University, Shenzhen 518057, China;
3. State Key Laboratory of Solid Lubrication, Lanzhou Institute of Chemical Physics, Chinese Academy of Sciences, Lanzhou 730000, China;
4. Key Laboratory of High Efficiency and Clean Mechanical Manufacture of MOE, School of Mechanical Engineering, Shandong University, Jinan 250061, China;
5. State Key Laboratory for Manufacturing System Engineering, School of Mechanical Engineering, Xi'an Jiaotong University, Xi'an, 710049, China;
6. Henan Key Laboratory of Intelligent Manufacturing Equipment Integration for Superhard Materials, Henan Mechanical and Electrical Vocational College, Zhengzhou 451191, China

Received 17 January 2024; accepted 4 April 2024

Abstract: High-entropy alloys (HEA) are novel materials obtained by introducing chemical disorder through mixing multiple-principal components, performing rather attractive features together with charming and exceptional properties in comparison with traditional alloys. However, the trade-off relationship is still present between strength and ductility in HEAs, significantly limiting the practical and wide application of HEAs. Moreover, the preparation of HEAs by trial-and-error method is time-consuming and resource-wasting, hindering the high-speed and high-quality development of HEAs. Herein, the primary objective of this work is to summarize the latest advancements in HEAs, focusing on methods for predicting phase structures and the factors influencing mechanical properties. Additionally, strengthening and toughening strategies for HEAs are highlighted, thus maximizing their application potential. Besides, challenges and future investigation direction of HEAs are also identified and proposed.

Key words: high entropy alloys; phase structure prediction; mechanical response; strengthening and toughening strategy; density functional theory

1 Introduction

Scanning the civilization history of human from stone age to bronze age, iron age and steel age, etc., every major advance of materials contributed to the significant progress of human development. Human beings are progressing gradually with the invention of new materials. In some sense, the development history of human beings could be defined as that of materials. Particularly, entropy played the most critical role in advancing the development of materials. Detailly, the configurational entropy greeted enhanced trend with the evolution of advanced materials, progressing the low entropy materials (traditional materials) to medium entropy materials, further to high entropy materials (HEM). HEM is a novel material obtained by introducing chemical disorder through mixing multiple-principal components, and thus, HEM is also named as multi-principal component materials, multi-component materials,

Corresponding author: Jia-lin SUN, Tel:+86-15686217698, E-mail: sunjialin@sdu.edu.cn
https://doi.org/10.1016/S1003-6326(25)66804-X

high-concentration complex materials, and composition complex materials, etc.

As demonstrated in Fig. 1, during the past decades, HEM has evolved from initial high entropy alloy to high entropy steel, high entropy high-temperature alloys, high entropy thin films, high entropy polymers, high entropy intermetallic compounds, high entropy ceramics, and high entropy cemented carbides, etc. Compared with traditional materials, HEM, providing multi-dimensional compositional space, was reported to perform rather attractive features together with charming and exceptional properties. HEA exhibited outstanding specific strength, excellent ductility and fracture toughness, and wear/oxidation/corrosion resistance [1−6], as well as superior high-temperature mechanical responses and thermal stability, exceeding those of conventional alloys as a function of the so-called four core effects: thermodynamic high-entropy effect, structural lattice distortion effect, kinetic hysteresis diffusion effect, and “Cocktail” effect on properties [7,8].

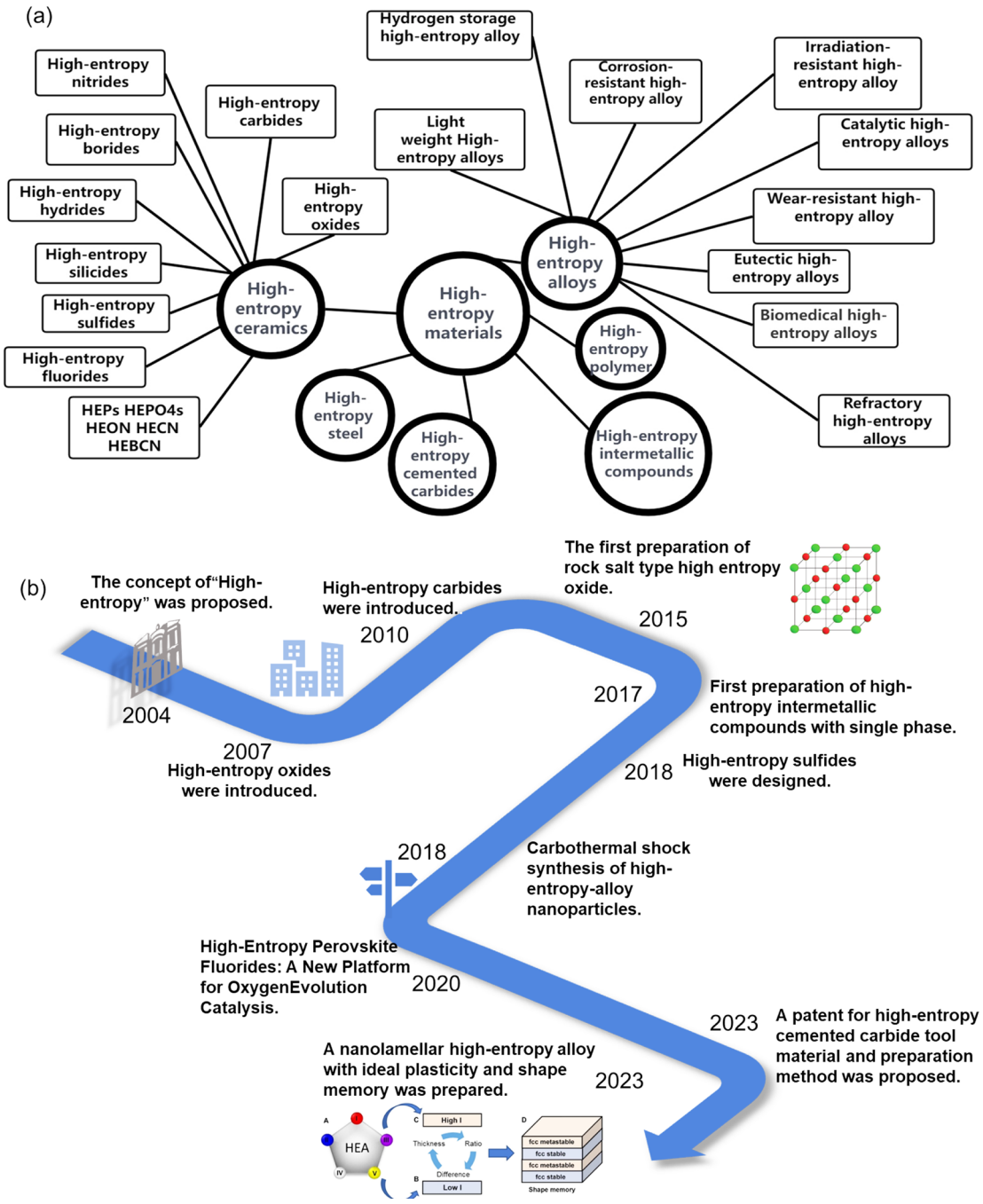

Fig. 1 Types (a) and development history (b) of high-entropy material [4]

(1) Thermodynamic high entropy effect is the base of the other three effects of HEA. Generally, the traditional alloy possesses the configurational entropy values much lower than that of HEA. Theoretically, the number of formed phases increases with the number of components. However, this is not suitable in case of HEA. Solid solution enjoys much higher configurational entropy in comparison with intermetallic compounds, resulting in the forming tendency of solid solution other than intermetallic compounds based on the principle of maximum entropy production. It is suggested that the high entropy effect renders the higher compatibility among multi-principal components, lowering the possibility of the occurrence of terminal solid solutions and intermetallic compounds. Therefore, HEAs tend to form single phase solid solution structure, enhancing the strength and plasticity of the alloy through solid solution strengthening effect.

(2) Structural lattice distortion effect of HEA originates from the traditional solid solution strengthening. HEA possesses crystal lattice composed of multi-atomic size multi-elements randomly occupying the lattice sites, thus inevitably resulting in severe lattice distortion. Moreover, the differences in bonding energy and crystal energy are also the factors causing lattice distortion. Actually, amorphous phase structure would give excessive lattice distortion energy formed because of exaggerated atomic size. The lattice distortion influenced the properties of HEA through generating strain and stress fields. For instance, during the plastic deformation process, lattice distortion would significantly impede dislocation movement, achieving prominent solid solution strengthening.

(3) Kinetic hysteresis diffusion effect refers to the phenomenon that the diffusion in HEA system is much slower than that in conventional alloy. However, the sluggish diffusion may not necessarily be applicable to all HEAs. The preliminary study conducted by TSAI et al [9] provided evidence for the sluggish diffusion observed in the $CoCrFeNiMn_{0.5}$ alloy through the calculation of tracer diffusion coefficients based on interdiffusion data. Subsequent research conducted by VAIDYA et al [10−12] on CoCrFeNi and CoCrFeMnNi alloys indicates that diffusion may be slow at inverse homologous temperatures, but not necessarily at absolute temperatures. In addition, some experimental investigations have indicated that this effect may not be accurately applicable to CoCrFeNi and CoCrFeMnNi HEAs [13−15]. Therefore, the generalization of the kinetic hysteresis diffusion effect to all HEAs may not be appropriate.

(4) “Cocktail” effect denotes that unexpectedly remarkable composite properties could be obtained in HEA through judiciously selecting the principal elements with specific properties. This concept is actually the extension of the idea of composite effect. The final property of HEA is not limited to the sum of the properties in individual elements, and is desired and higher than the combined one. In other words, compared with traditional interface regulation, HEA can achieve fine regulation of structure and properties by means of element type and concentration regulation. For example, the $CoCrCuNiAl_x$ HEA changed from FCC to FCC+BCC and then to BCC structure as a function of enhanced Al content. The inclusion of high melting point elements such as tungsten and vanadium will improve the high-temperature properties of the alloy, whereas the selection of Al and Si can enhance the oxidation resistance of the resulting HEA.

Figure 2 demonstrates the keyword co-occurrence diagram and plot of strength versus elongation of HEA and other damage-tolerant materials on record. HEA enjoys proud history since it was invented in 2004 [16]. As illustrated in Fig. 2(a), the high frequency research objects of HEAs rank as mechanical properties, solid solution, alloy design, etc., which are focused critically on the state-of-art engineering structural application of HEA. It has been generally accepted that HEA possessed enhanced mechanical responses and the chemical/thermal/electrical properties in comparison with conventional alloys. Especially, as shown in Fig. 2(b), HEA yielded much improved toughness and strength than most damage-tolerant materials including traditional alloys, ceramics, etc. However, whilst initially appealing, only very few of them, to date has been commercialized and produced on an industrial scale. The conflict of strength and ductility is also inevitable in HEA system. Simultaneously further enhanced strength and ductility are highly demanded for HEA supporting the advanced manufacturing.

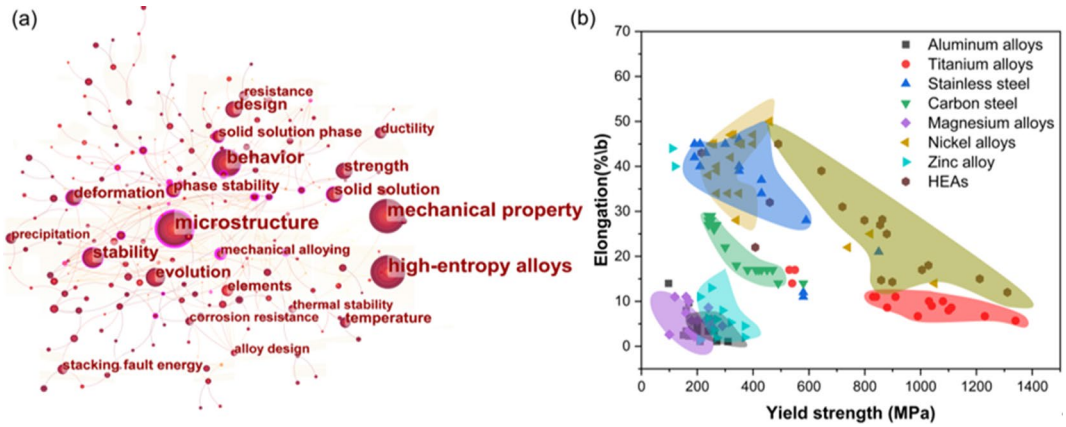

Fig. 2 High-entropy alloys keyword co-occurrence diagram (a); Comparison of yield strength and elongation of high-entropy alloys and conventional alloys (b)

Based on above discussion, HEAs do yield superior structure and properties to the traditional materials. However, the trade-off relationship is still present between strength and ductility in HEAs, significantly limiting the practical and wide application of HEAs. Moreover, the preparation of HEAs by trial-and-error method was time-consuming and resource-wasting, hindering the high-speed and high-quality development of HEAs. Herein, the primary objective of this current review is to summarize the latest advances of HEAs, mainly regarding the phase structure prediction and mechanical properties, highlighting the strengthening/toughening strategies in HEAs, so as to maximize the application of HEAs. Besides, challenges and future investigation direction of HEAs are also identified and proposed.

2 Development history and research highlights

There is a lack of a unified definition for HEAs, as the existing definitions are diverse and varied. The earliest definition categorizes HEAs as alloys composed of at least five primary metallic elements, each of which has an atomic percentage varying from 5% to 35% [16]. Another way to define it is from the perspective of entropy, where an alloy with molar configuration entropy (ΔS_{conf}) >1.61R is referred to as a HEA [17]. In addition, it was proposed that any alloy meeting ΔS_{conf}>1.5R can be referred to as a HEA [18].

To investigate the trajectory of HEAs research over the past 19 years, from 2004 to 2023, we employed the Web of Science search engine as a research tool. The growth of publications in the field of HEAs over years is bar-charted in Fig. 3. One can see that the number of published articles on HEAs experiences explosive growth. In order to better understand the recent progress of HEAs, we have compiled some major research results about HEAs in Fig. 4.

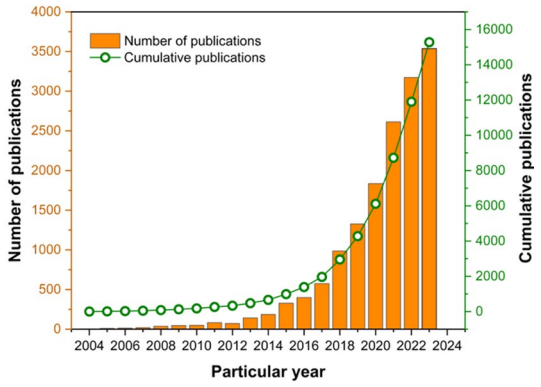

Fig. 3 Number of publications on HEA, along with cumulative publications over years from 2004 to 2023

Regarding the origin of HEAs, it can be traced back to YEH et al [16] proposing the concept of HEAs in 2004. Since then, research on HEAs has flourished. Multicomponent nanoparticles have an urgent need in many fields, but they have been limited by the lack of effective strategies to synthesize such structures. CHEN et al [19] have developed a library composed of five elements, which provides important insights into the formation of alloys and phase segregation at the nanoscale. After that, a versatile and simple solution

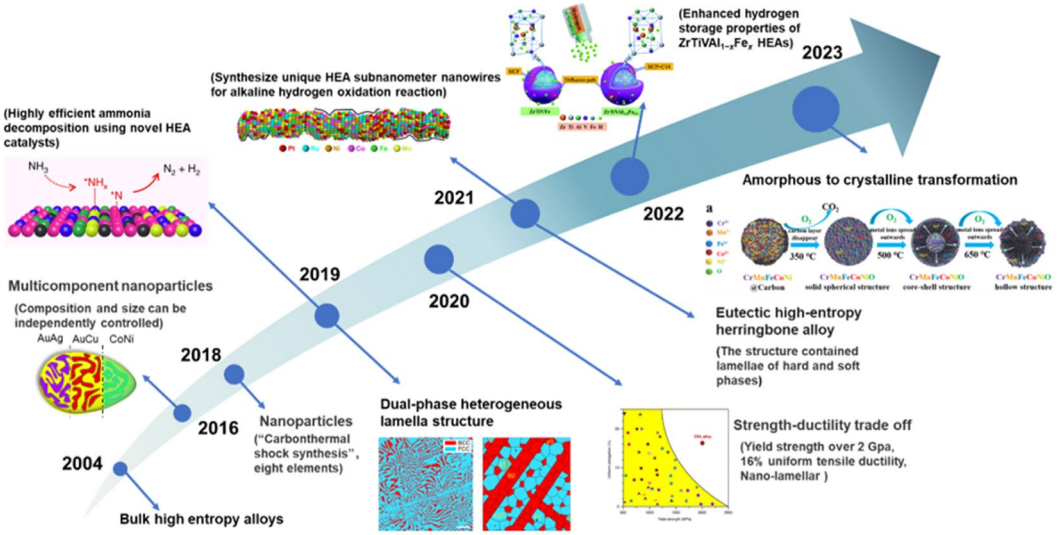

Fig. 4 Progress of high-entropy alloys [16−23,26−31]

has been proposed to address the challenge of fabricating the nanoparticles from the multiple incompatible elements at the nanoscale in 2018 [20]. The controllable incorporation of the multiple immiscible elements into a single nanoparticle will bring more variations and potential to the performance of nanoparticles. As we all know, eutectic high entropy alloys (EHEAs) as a novel alloy with multi-principal elements, which provide more possibilities for HEAs to have superior comprehensive mechanical properties. In 2019, SHI et al [21] successfully prepared $AlCoCrFeNi_{2.1}$ EHEA with excellent strength and ductility. One year later, this research team used a unique solidification microstructure control method to solidify the uniform eutectic structure in EHEAs into a hierarchically organized herringbone structure [22]. The prepared self-buffering herringbone EHEAs exhibit an ultrahigh uniform tensile elongation (~50%), which is three times that of non-buffering EHEAs, without sacrificing strength.

In 2020, FAN et al [23] successfully developed a novel HEA with ultra-high strength (over 2 GPa) and high ductility (16%) by utilizing the design concept of coherent nanolamellar architectures. Recently, researchers have achieved an EHEA with a uniform elongation of 35% and a fracture true stress close to 2 GPa by utilizing the strain hardening capability of the two phases in eutectics through phase selection recrystallization [24]. Significant progress has been made in the development of medium-entropy alloys (MEAs) with high strength and high ductility. DU et al [25] achieved a heterogeneous grain structure through low-temperature rolling and high-temperature annealing, resulting in CoCrNi-based medium-entropy alloys (MEAs) exhibiting ultra-high strength (tensile strength of 2.2 GPa) and uniform elongation (13%). These signify a significant breakthrough in achieving high strength and high ductility in alloys, offering a new paradigm for designing HEAs with excellent mechanical properties.

Ammonia is a promising liquid fuel for hydrogen storage, but it cannot be widely used in industry because its catalyst ruthenium (Ru) is a precious metal. The prepared CoMoFeNiCu HEA nanoparticles exhibit stronger catalytic activity and stability for ammonia decomposition compared with the metal Ru [26]. In 2021, the PtRuNiCoFeMo HEA nanowires catalyst for alkaline hydroxide reaction exhibited high activity and promising resistance to CO poisoning compared with the traditional PtRu/C and Pt/C catalysts [27].

Hydrogen has great promise to revolutionize in the energy field as a potential renewable energy source and an alternative to fossil fuels due to its abundant storage and cleanliness. The characteristics of multiple principal elements of HEAs increase the binding energy of the matrix and hydrogen, which is conducive to the improvement of hydrogen storage performance [28]. Since KAO et al [29] introduced the hydrogen storage performance of $CoFeMnTi_xV_yZr_z$ HEA in 2010,

many scholars have discovered the promising application of HEAs in the field of hydrogen storage. The ZrTiVAl lightweight high-entropy alloy (LHEA) has shown great potential in the field of hydrogen storage due to its considerable capacity, easy activation and fast hydrogenation rate [30]. The fabricated $ZrTiVAl_{1-x}Fe_x$ exhibits excellent hydrogenation rates even at room temperature. Recently, researchers have proposed a method for amorphous to crystalline transition, which can realize the synthesis and regulation of high-entropy metal oxides simultaneously [31].

3 Methods for predicting phase structure of high-entropy alloys

HEAs have triggered many scholars' interest due to their outstanding mechanical properties that largely depend on the selection among three phases: solid solution (SS), intermetallic compound (IM), and mixed SS and IM (SS+IM) [32]. The desirable properties of HEAs are often attributed to the presence of the single SS phase. Conversely, the presence of a brittle IM phase has a detrimental effect on the ductility of HEAs [33]. The traditional trial-and-error method for the preparation of HEAs not only consumes a lot of time and energy of researchers, but also has great uncertainty in the mechanical properties of the synthesized HEAs. It is evident that the conventional preparation technique is insufficient to meet current demands, and thus the critical need to expedite the practical implementation of HEAs through phase structure prediction is emphasized.

3.1 ΔH_{mix}−δ criterion

Scholars have preciously studied the influence of atomic size, crystal structure, valence electron concentration and electronegativity of elements in binary alloy system on solid solutions, and proposed the Hume−Rothery criterion [34]: (1) For alloys with atomic-size differences between their components exceeding 15%, it is highly unlikely to create a substitution solid solution; (2) When there is a significant variation in the electronegativity of the alloying elements, the solid solubility becomes minimal, leading to the formation of stable compounds within the alloy.

ZHANG et al [35] creatively extended the Hume−Rothery rulers to the field of HEAs. After analyzing the mixing enthalpy (ΔH_{mix}) and atomic radius difference (δ) of a large number of cast HEAs, the ΔH_{mix}−δ criterion was proposed to study the phase formation rules of HEAs. Here, ΔH_{mix} characterizes the chemical compatibility among the principal atoms in HEAs. According to the regular melt model [36], the ΔH_{mix} can be expressed as

$$\Delta H_{\mathrm{mix}}=\sum_{i=1,i\neq j}^{n}\Omega_{ij}c_ic_j \tag{1}$$

where Ω_{ij} is the regular melt-interaction parameter of the ith and jth principal elements; c_i an c_j are the atomic percentages of the ith and jth principal elements, respectively; n is the number of primary elements.

δ indicates the degree of lattice distortion of the alloy structure, and its expression is [37]

$$\delta=\sqrt{\sum_{i=1}^{N}c_i\left(1-\frac{r_i}{\overline{r}}\right)^2} \tag{2}$$

$$\overline{r}=\sum_{i=1}^{n}c_ir_i \tag{3}$$

where $\overline{r}$ is the average atomic radius of the principal element; r_i is the atomic radius of the ith principal element. The relationships of ΔH_{mix}−δ are presented in Fig. 5(a). The range of SS phase formation can be determined as follows: δ<6.5%, −15 kJ/mol<ΔH_{mix}<5 kJ/mol, and 12 J/(K·mol)< ΔS_{mix}<17.5 J/(K·mol).

3.2 VIC criterion

GUO and LIU [38] enhanced and supplemented previous study, through adding two parameters, VEC (valence electron concentration) and $\Delta\chi$ (electronegativity difference). VEC has been verified critical in determining the phase stability of IM [39]. It was proposed to use VEC as a criterion to distinguish the BCC phase from the FCC phase [40]. The VEC is defined as the number of valence electrons in the alloy, and its expression is

$$\mathrm{VEC}=\sum_{i=1}^{n}c_i\left(\mathrm{VEC}\right)_i \tag{4}$$

where $(VEC)_i$ is the VEC for the ith element. As shown in Fig. 5(b), at VEC > 8.0, single-phase FCC exists; at VEC < 6.87, only the BCC phase exists; while both FCC and BCC phase coexist in the region of 6.87 <VEC< 8 [40].

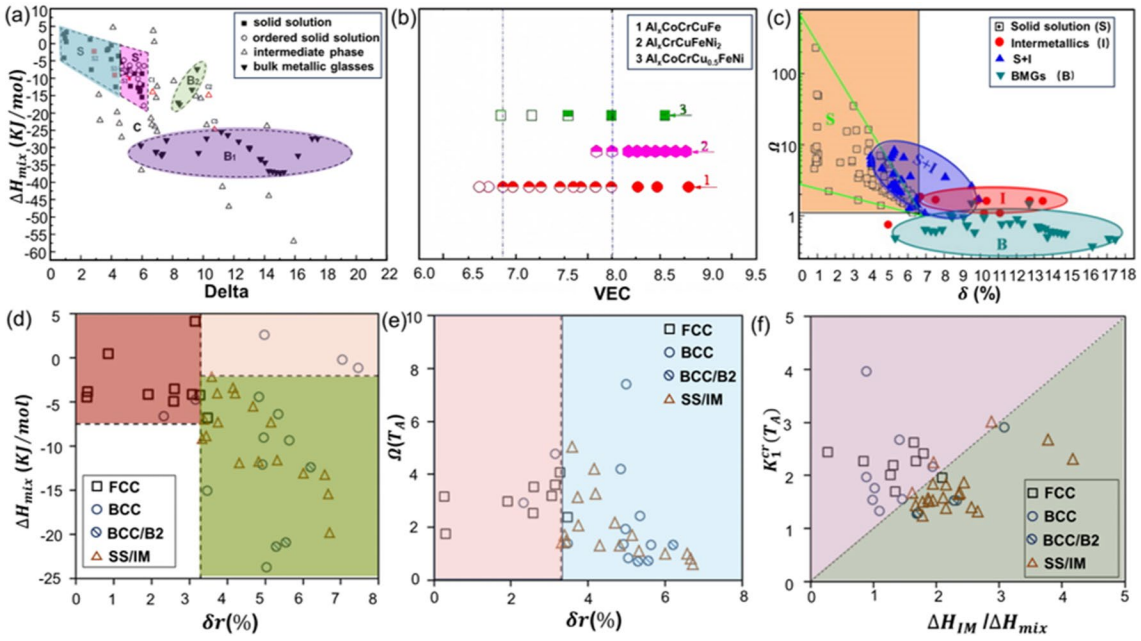

Fig. 5 Relationship between δ and ΔH_{mix} for MHAs and typical multicomponent bulk metallic glasses (a) [35]; Relationship between VEC and FCC, BCC phase stability for HEA systems (b) [40]; Relationship between parameters Ω and δ for multi-component alloys (c) [43]; ΔH_{mix}−δr relationship (d), $\Omega(T_A)$−δr relationship (e) and $k_1^{Cr}(T_A)$ − $\Delta H_{IM}/\Delta H_{mix}$ plots (f) for annealed HEAs with different phase contents after annealing [44]

3.3 ΔH_{mix}−δ−VEC criterion

It was suggested that atomic size greatly affects the diffusion coefficient of high-entropy solid solutions [41]. Inspired by this, JIANG et al [42] proposed that the parameters of atomic size difference (δ), ΔH_{mix} and VEC were integrated to predict the formation of the single-phase SS structure HEAs. It was proposed that single phase FCC SS prefers to form in the case of δ<4.27%, −7.27 kJ/mol<ΔH_{mix}<4 kJ/mol and VEC>8, while the single phase BCC SS prefers to form in the case of δ <4.27%, −7.27 kJ/mol<ΔH_{mix}<4 kJ/mol and VEC < 6.87.

3.4 Ω−δ criterion

It is noted that both positive ΔH_{mix} and negative ΔH_{mix} have the same effect on limiting the formation of SS phases [43]. The finding indicates that high ΔS_{mix} increases the chaos of the alloy system, i.e., different atoms are randomly distributed in the crystal lattice. As we all know, as the temperature increases, the effect of ΔS_{mix} becomes more pronounced. The high $T\Delta S_{mix}$ is conducive to the formation of the solution phase, which also indicates that the $T\Delta S_{mix}$ can be used as an indicator to characterize the driving force of the formation of the SS phase. After the analysis, it was proposed that combining the effect of $T\Delta S_{mix}$ with the effect of ΔH_{mix} could describe the stability of the SS phase in HEA, and a new parameter Ω was proposed. The expression for Ω is as follows:

$$\Omega = \frac{T_m \Delta S_{mix}}{|\Delta H_{mix}|} \tag{5}$$

where T_m is the thermodynamic temperature. Figure 5(c) shows the relationship between Ω and δ. In Region S, HEA has a small atomic size difference and a large Ω value, which indicates a low strain energy due to lattice distortion. And in this region, the effect of ΔS_{mix} on the formation of SS is greater than that of ΔH_{mix}. This is a reasonable explanation for the formation of the SS phase only in Region S. In the Region S+I (Fig. 5(c)), not only the SS phase is formed, but also some ordered compounds could precipitate in the HEAs system. In this region, atomic size differences and the effect of ΔH_{mix} have enabled the formation of IM and some other ordered phases in the HEAs system. In conclusion, when the Ω≥1.1 and δ≤6.6%, the HEAs tend to form a SS phase, and when δ≤3.6%, only the SS phase is formed in the HEAs.

3.5 $k_1^{Cr}(T)$ criterion

After examining the relationship between enthalpy of formation (ΔH_{IM}), enthalpy of mixing (ΔH_{mix}), entropy of formation (ΔS_{IM}) and mixed entropy (ΔS_{mix}), $k_1^{Cr}(T)$ was proposed as criterion to predict the phase structure of HEAs [44]. The expression for $k_1^{Cr}(T)$ is

$$k_1^{Cr}(T) = -\frac{T\Delta S_{mix}}{\Delta H_{mix}}(1-k_2)+1 > k_1 = \frac{\Delta H_{IM}}{\Delta H_{mix}} \quad (6)$$

$$k_2 = \frac{\Delta S_{IM}}{\Delta S_{mix}} \quad (7)$$

where $0<k_2<1$.

When the temperature is constant, the condition for the formation of the SS phase in the alloy is

$$k_1^{Cr}(T) > \Delta H_{IM}/\Delta H_{mix} \quad (8)$$

It is shown that the new criterion gives an improved ability to predict whether solid solution or intermetallic phases will form at a given temperature compared to earlier criteria (Fig. 5(f)). However, the new criterion still cannot predict what type of SS phase will form.

3.6 $\Delta S_{config}/\Delta S_{fusion}-\Delta S_\sigma/k$ criterion

The molar configuration entropy (ΔS_{config}) of a phase is a critical parameter for phase formation. RAGHAVAN et al [45] proposed the $\Delta S_{config}/\Delta S_{fusion}-\Delta S_\sigma/k$ criterion based on the statistical analysis of HEAs with equal atomic ratio and non-equal atomic ratio. $\Delta S_\sigma/k$ is widely used for the analysis of bulk metallic glasses, which was proposed by MANSOORI et al [46]. These three parameters can be expressed as

$$\Delta S_{config} = -R\sum_{i=1}^{n} x_i \ln x_i \quad (9)$$

$$\Delta S_{fusion} = \sum_{i=1}^{n} \Delta S_{f,i} \quad (10)$$

$$\frac{\Delta S_\sigma}{k} = [1.5(\zeta^2-1)y_1 + 1.5(\zeta-1)y_2 - (0.5(\zeta-1)(\zeta-3)+\ln\zeta)(1-\zeta)y_3] \quad (11)$$

where x_i is the mole fraction of atom i; ζ is the packing fraction; y_1, y_2 and y_3 are the dimensionless parameters. The ΔS_{fusion} for all compositions was assessed in order to examine the range of values they displayed. The $\Delta S_{f,i}$ values represent the entropy of fusion for the individual elements of the alloy. $\Delta S_\sigma/k$ is referred to as the mismatch entropy, which represents the main topological/strain parameter controlling phase formation. The findings suggest that the formation of SS in alloys containing multiple components are more likely to occur when the ratio of $\Delta S_{config}/\Delta S_{fusion}>1$ for equiatomic alloys and >1.2 for non-equiatomic alloys.

3.7 Λ criterion

As we mentioned earlier, an elevated ΔS_{mix} promotes the formation of disordered solid solution (DSS). Previous studies have found that a high δ value exhibits the opposite effect and promotes the formation of compounds (δ^2 is proportional to the strain energy) [43]. In consideration of this, a purely geometrical parameter ($\Lambda=\Delta S_{mix}/\delta^2$) to predict the formation of DSS was proposed [47]. The Λ-parameter for an alloy can be determined solely based on geometric data, such as the configuration on a lattice and the size of the atoms. One overarching pattern indicates that for high value of the Λ-parameter, the DSS formation is favored, while a decrease in this parameter leads to the observation of FCC-based ordered structure ($L1_2$) followed by BCC-based ordered structure (B2). At lower values of Λ, the formation of complex compounds occurs, such as σ-phase and Laves phase [47]. In summary, when $\Lambda>0.96$, HEAs tend to form a single SS phase; when $0.24<\Lambda<0.96$, a duplex SS phase is formed in the HEAs; when $\Lambda<0.24$, IM tends to form in HEAs.

3.8 $\Delta G_{F-B}-\phi$ criterion

In accordance with the second law of thermodynamics, the phase composition of a HEA can be anticipated by evaluating the Gibbs free energies of various states within the same alloy system. Based on this, YIN et al [48] proposed a novel strategy for further predicting the SS phase structure of HEAs by utilizing the Gibbs free energy difference between BCC and FCC phases (ΔG_{F-B}), which can be express as

$$\Delta G_{F-B} = \sum_{i=1}^{n}\sum_{j=i+1}^{n} 4\left(\Delta H_{ij}^{FCC} - \Delta H_{ij}^{BCC}\right)x_i x_j + \sum_{i=1}^{n} x_j\left(G_i^{FCC} - G_i^{BCC}\right) \quad (12)$$

where $(\Delta H_{ij}^{FCC} - \Delta H_{ij}^{BCC})$ represents the mixing enthalpy difference of the equimolar binary alloys

with lattice structures of FCC and BCC, and $(G_i^{FCC} - G_i^{BCC})$ denotes the Gibbs free energy difference of the element i with lattice structures of FCC and BCC. Additionally, the ratio parameter ϕ has been proposed to reduce the impact of B2 and $L1_2$ on prediction accuracy. ϕ represents the content ratio of the A to B elements (A includes Al and Ti, while B includes Ni and Co).

The statistical findings indicate that HEAs tend to form FCC SS phase when $-1.13<\Delta G_{F-B}<0.21$, while for the formation of BCC SS phase in HEAs, the ΔG_{F-B} value tends to be 0.21−1.18. The ΔG_{F-B} values of the HEAs that form a SS structure of both BCC and FCC range from 0.24 to 0.72. Specifically, in the overlapping region of FCC/FCC+BCC, HEAs tend to form $L1_2$ phase when the ϕ value is less than 0.33. However, when the ϕ value is greater than 0.72, B2 phase can be formed in the overlapping region of BCC/BCC+FCC.

3.9 Machine learning methods

As a part of artificial intelligence, machine learning (ML) combined with materials science provides new means and directions for materials science research [49,50]. Most of the previous studies on the prediction of HEAs phase structure used density functional theory (DFT) calculations to obtain relevant parameters. However, this method is cumbersome to calculate, and the prediction results are highly uncertain. Machine learning is a powerful tool for predicting the phase structure and mechanical properties of HEAs.

A systematic framework that utilizes a genetic algorithm (GA) to efficiently select the ML model and materials descriptors was proposed [51]. The enhanced classification model achieves an accuracy up to 88.7% in distinguishing between solid-solution and non-solid-solution HEAs, and further attains recognition accuracy of 91.3% for identifying BCC, FCC, and dual-phase HEAs. In addition, an active learning method was used to select several HEAs with the greatest classification uncertainties. These alloys were then synthesized and identified, and added to the initial dataset to iteratively enhance the machine learning model. This approach can be applied as a universal algorithm for choosing material descriptors and machine learning models for a range of material issues, such as classifying and optimizing specific properties. ZHAO et al [52] used ML to combine elemental characteristics with long-term ordering and obtained 87% of prediction accuracy. This data-driven approach can speed up the identification of possible compositions by correlating elemental properties with metastable states.

A new machine learning-based design method for HEAs has greatly improved the design efficiency of HEAs, and a variety of new high-entropy Invar alloys have been successfully designed [53]. The learning framework integrated ML with DFT, thermodynamic calculations, and experimental feedback (Fig. 6). HEA generative

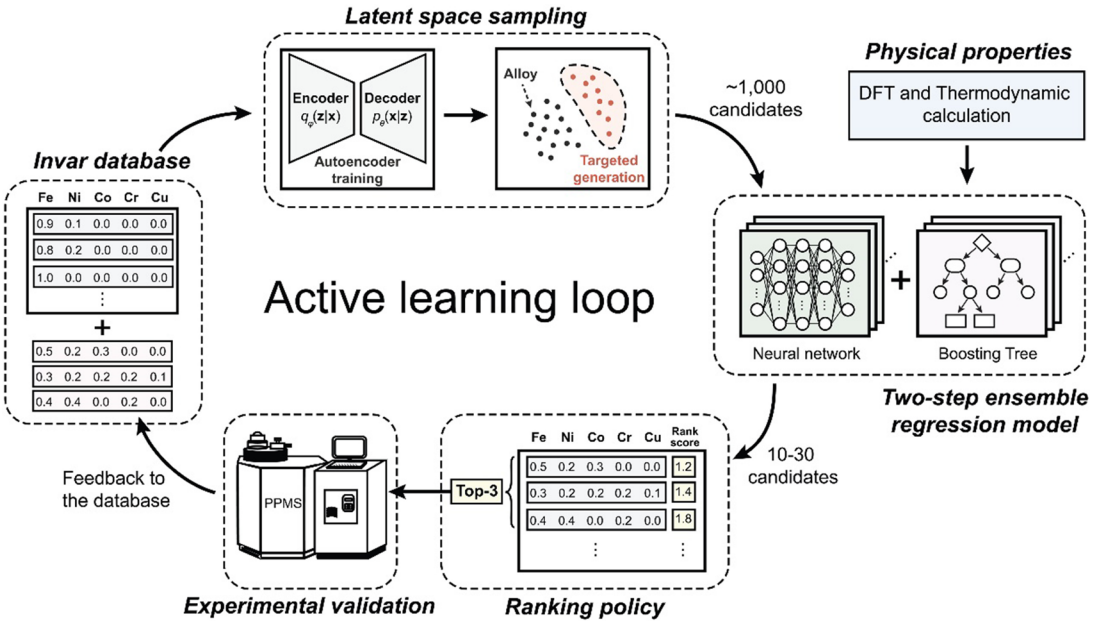

Fig. 6 Learning framework intergrating ML with DFT, thermodynamic calculations, and experimental feedback [53]

alloy design (HEA-GAD) approach is based on a generative model. First of all, the HEA-GAD conducts a thorough search for putative Invar alloys using generative model (GM), mathematical modeling, and sampling. Previous research has indicated that GM has acquired an efficient method for representing high-dimensional data, which not only offers a direct visualization of the data but also transforms the search in high-dimensional design space into a search in low-dimensional design space [54]. Then, in order to learn more about the thermal expansion coefficient (TEC) of the alloy components, a two-stage ensemble regression model was employed. The first stage involved a combination-based regression model aiming at rapid and large-scale component combination inference. Ultimately, the TEC values of the initial three chosen candidate materials were ascertained through experiments using a physical property measurement system. The outcomes of these experiments subsequently contribute to a training database for the subsequent active learning iteration [53].

4 Mechanical properties of high-entropy alloys

4.1 Hardness

There is a wide range of hardness levels for HEAs, depending on the alloy system and processing technology. The choice of alloy system, manipulation of composition ratios within the alloy system, and selection of alloy processing methods are essential factors in determining the hardness of HEAs [55].

4.1.1 Influence of alloying on hardness

The proportion of the alloying elements significantly influences the microstructure and mechanical characteristics of HEAs, making them a focal point of interest in the field of metallurgy. It was proposed that the deformation of the crystal lattice and potential reinforcement of the bond strength between Al and other elements contribute to the observed increase in the alloy's hardness [56]. The hardness of $Al_xCoCrFeNi$ HEA demonstrates a positive correlation with the concentration of Al, culminating in a peak hardness of HV 740 when the value of x is 3 [56]. The as-cast $FeCoNiCrCu_{0.5}Al_x$ (x=0.5, 1.0, 1.5) HEAs exhibited hardness values of HV 289.5, 665, and 618.5, respectively [57]. This phenomenon occurs because the presence of Al promotes the transition of HEAs from the relatively soft FCC phase to the harder BCC phase. Additionally, the relatively large atomic radius of Al leads to significant lattice distortion, thereby enhancing its hardness. Furthermore, it is indicated that the addition of non-metallic elements such as C or Si is a viable method for enhancing the hardness of HEAs. The hardness of $Fe_{2.5}CoNiCuSi_x$ (x=0.1−0.3) HEA exhibits a continuous increase for $x\leq0.25$, followed by a subsequent decrease, reaching HV 491.2 at x=0.3 [58].

4.1.2 Influence of structure on hardness

The phase structure also serves as a significant factor influencing the hardness of HEAs. The preceding passage indirectly demonstrates that BCC phase HEAs generally exhibit superior hardness compared to HEAs with the same composition but in the FCC phase. In addition, grain size is also an important factor in hardness. It has been suggested that the FCC phase $Al_{20}Li_{20}Mg_{10}Sc_{20}Ti_{30}$ HEAs with a grain size of 12 nm exhibited a hardness up to 5.8 GPa [59]. After annealing at 500 °C for 1 h, its structure transforms into an HCP phase with a grain size of 26 nm, resulting in a reduction in hardness of 4.9 GPa. EDALATI et al [60] succeeded in achieving an ultra-high hardness of HV 1030 by introducing nanograins into a dual-phase AlCrFeCoNiNb HEA. The significant increase in hardness can be attributed not only to the creation of nanograins averaging 10 nm in size, but also to the emergence of dislocations, interfaces, and spinodal-like elemental decomposition. It has been suggested that the presence of dislocations and their contribution to ultra-high hardness should be caused by the effect of lattice distortion on the inhibition of dislocation mobility.

4.1.3 Influence of annealing treatment on hardness

During the annealing process, the presence of precipitates can frequently lead to a notable enhancement in the hardness of HEAs. The phenomenon of aging hardening is often associated with the process of precipitation [55]. This intense high-temperature aging hardening phenomenon provides a new route to improve the hardness of HEAs.

Two HEAs, $Al_xCrFe_{1.5}MnNi_{0.5}$ (x=0.3 and 0.5), exhibit a notable age-hardening effect at elevated temperatures [61]. The as-cast $Al_{0.3}CrFe_{1.5}MnNi_{0.5}$ alloy demonstrates the ability to achieve a maximum hardness of HV 850 at 600 °C for 100 h,

while the $Al_{0.5}CrFe_{1.5}MnNi_{0.5}$ alloy can achieve an even higher hardness of Hv 890. It is suggested that the aging hardening can be attributed to the formation of the $Cr_5Fe_6Mn_8$ (ρ phase) structure in $Al_xCrFe_{1.5}MnNi_{0.5}$ HEAs. Furthermore, following the process of aging, the hardness of $Al_{0.3}CoCrFeNi$ alloy was increased by 65%, while the hardness of $Al_{0.3}CoCrFeNiMo_{0.1}$ and $Al_{0.3}CoCrFeNiTi_{0.1}$ was increased by more than 80% [62]. Different precipitated phase structures were observed in the three HEAs after aging. Precipitated (Ni,Al)-rich B2 phase and (Ni,Co,Ti)-rich B2 phase were the reasons for the improvement of hardness for $Al_{0.3}CoCrFeNi$ and $Al_{0.3}CoCrFeNiTi_{0.1}$, respectively. At the same time, the double precipitation of (Ni,Al)-rich phase and (Cr,Mo)(Co,Fe,Ni) σ phase explained the significant aging hardening of $Al_{0.3}CoCrFeNiMo_{0.1}$.

4.2 Elevated-temperature properties

The elevated-temperature properties of the HEAs were also extensively studied. It is the outstanding elevated-temperature properties that make HEAs have great application potential in high-temperature fields. It is proposed that due to the presence of sluggish diffusion effect and second-phase strengthening, HEAs may exhibit sustained high levels of strength at elevated temperatures [63].

4.2.1 Influence of sluggish diffusion effect

The sluggish diffusion effect in some HEAs results in a slower diffusion rate compared to traditional alloys. This phenomenon has been commonly considered as a reason for the exceptional strength at high temperatures and the impressive structural stability of HEAs [64].

Two refractory high-entropy alloys (RHEAs), namely $Nb_{25}Mo_{25}Ta_{25}W_{25}$ and $V_{20}Nb_{20}Mo_{20}Ta_{20}W_{20}$, exhibit significantly higher yield stress compared to Haynes 230 alloy across all examined temperatures, with temperatures exceeding 800 °C showing even higher yield stress than Inconel 718 superalloy [65]. The notable ability of RHEAs to withstand high-temperature softening, in contrast to super-alloys, is attributed to the sluggish diffusion of elements within the HEAs at temperatures reaching 1600 °C [65].

The preservation of structural stability is a critical concern in high-temperature environments. HEAs typically exhibit favorable structural stability when subjected to elevated temperatures. TASI et al [66] prepared a metallic diffusion barrier layer, NbSiTaTiZr HEA, which exhibited thermal stability comparable to ceramic barrier layers. The excellent stability of the amorphous structure in NbSiTaTiZr is suggested to be attributed to the sluggish diffusion effect.

4.2.2 Influence of second phase strengthening

It has been suggested that the incorporation of stable second phase can enhance the elevated-temperature properties of HEAs. $Re_{0.1}Hf_{0.25}NbTaW_{0.4}C_{0.25}$ RHEAs exhibit an excellent high-temperature compressive strength (1026 MPa at 1450 °C, and 523 MPa at 1700 °C) and softening resistance [67]. The excellent elevated-temperature properties can be attributed to the high-entropy MC-type carbides, which have high melting point and elevated-temperature strength [68]. A novel $Al_{17}Ni_{34}Ti_{17}V_{32}$ EHEA has demonstrated higher high-temperature hardness ($HV_{0.3}$ 459 at 800 °C, and $HV_{0.3}$ 446 at 900 °C) and yield strength (1209±24) MPa at 600 °C, (1016±22) MPa at 700 °C, and (786±18) MPa at 800 °C) compared to most commonly reported RHEAs [69]. This phenomenon arises from the incorporation of a stable Heusler-type ordered ($L2_1$) phase in $Al_{17}Ni_{34}Ti_{17}V_{32}$, characterized by a significant proportion of low-density elements and the creation of a low lattice mismatch eutectic phase interface. Furthermore, the novel $(Ni_2Co_2FeCr)_{92}Al_4Nb_4$ HEAs exhibit a yield strength exceeding 720 MPa at 760 °C [70]. In the $(Ni_2Co_2FeCr)_{92}Al_4Nb_4$ alloy, high-density coherent $L1_2$ nano-precipitates with a composition of $(Ni,Co,Fe,Cr)_3(Al,Nb)$ are introduced, resulting in a lattice misfit of approximately 0.78%. It was proposed that the exceptional elevated-temperature properties exhibited by $(Ni_2Co_2FeCr)_{92}Al_4Nb_4$ is associated with its large lattice misfit and the shear mode of $L1_2$ precipitates.

4.3 Strength and ductility

There is a strong demand for high-strength materials in structural components to enhance load-bearing capacity while minimizing mass. In addition to strength, these materials should also exhibit favorable ductility and toughness to facilitate shaping into different forms and to prevent potential catastrophic failure during service [71]. Strength and ductility have always been mutually

exclusive, i.e., an increase in strength inevitably leads to the sacrifice of plasticity, and vice versa. Inferior ductility has become the "Achilles' heel" of high-strength metal materials, even HEAs with good comprehensive mechanical properties are no exception.

As a promising material in the field of metal materials, HEAs exhibit excellent strength and ductility. It was proposed that the remarkable strength and ductility of HEAs may be ascribed to the unique combination of strengthening mechanism such as partial slip, conventional octahedral slip, and deformation twinning [72]. Elemental composition is undoubtedly a crucial factor in the strength and ductility of HEAs.

4.3.1 Composition effect

Nb is a significant element that can contribute to the enhancement of strength and promote the development of eutectic structures [73]. It was proposed that the fracture and yield strength of $CoCrFeNiNb_x$ HEA demonstrated an increase with the higher content of Nb [74]. Similarly, CHANDA and DAS [75] systematically studied the effects of Nb addition on the mechanical properties of $CoCrFeNiNb_x$ ($0.45 \leq x \leq 0.65$). Among them, $CoCrFeNiNb_{0.5}$ exhibits ultra-high yield strength ((2060±5) MPa) and comparable compressive plasticity (17±0.51)%), while its strain hardening can reach (2200±10) MPa. It has been suggested that the increment of the strength can be attributed to the increase in the volume fraction of the Nb-rich Laves phase with the HCP structure with increasing the Nb content [74,75]. Additionally, the incorporation of nitrogen is an effective method for enhancing the strength of HEAs. Nitrogen-doped $CrMnFeVTi_6$ HEA demonstrates a yield strength up to 2729 MPa [76]. It was proposed that the introduction of N into the BCC phase can result in a yield strength increase of ~634 MPa/at.% [76]. The primary reason for the improvement in yield strength of nitrogen-doped $CrMnFeVTi_6$ is attributed to the interstitial solid solution strengthening caused by the presence of N. Additionally, the formation of Laves phases and TiN_x also contributes to the enhancement.

It has been suggested that the addition of La is one of the feasible methods for enhancing the strength of HEAs. The ultimate strength and yield strength of $(NbMoTiVSi_{0.2})_{100-x}La_x$ generally increase with the increasing amount of La added [77]. The ultimate strength and yield strength of $(NbMoTiVSi_{0.2})_{99.5}La_{0.5}$ are 2157 and 1929 MPa, respectively, and it also exhibits comparable fracture strain (15.28%).

4.3.2 Structure effect

The microstructure can manifest in various configurations, encompassing phase composition, grain size, dislocation density, twinning, stacking faults, as well as the size and dispersion of precipitates, among other characteristics [73]. A variety of microstructures have the potential to make HEAs exhibit different mechanical properties. For example, FCC HEAs tend to exhibit low strength and high ductility, while most of BCC HEAs exhibit high strength and inferior ductility.

Eutectic microstructure is a very typical type of microstructure in HEAs, and its formation is often related to ordered phases and compounds. SHI et al [21] successfully prepared $AlCoCrFeNi_{2.1}$ EHEA with excellent strength (~1.5 GPa) and ductility (~16% in elongation). The excellent mechanical properties can be attributed to two concurrent effects, i.e., the self-generated micro-crack-arresting mechanism and two-hierarchical constraint effect [21]. And a unique solidification microstructure control method was used to solidify the uniform eutectic structure in EHEAs into a hierarchically organized herringbone structure [22]. The prepared self-buffering herringbone EHEAs exhibit an ultrahigh uniform tensile elongation (~50%), which is three times that of non-buffering EHEAs, without sacrificing strength.

The mechanical properties of some HEAs are summarized in Table 1.

5 Strengthening and toughening of HEAs

5.1 Fine grain strengthening

The mechanism of fine-grain strengthening can be summarized as follows: grain boundaries hinder the dislocation movement during the deformation of the material. The reduced grain contributes to enlarged grain boundary area and further obstruction of dislocation motion [96], consequently dramatically improving the yield strength of the alloys. More grains would be contained in the unit volume giving finer grain, and thereby, the deformation would be evenly dispersed in more grains with external force applied on the materials [97].

Table 1 Mechanical properties of high-entropy alloys

Alloy	Processing method	Structure	Hardness/GPa	Yield strength/MPa	Ultimate tensile Strength/MPa	Elongation/%	Ref.
AlCoCrFeNi	AN (950 °C, 0 T field)	BCC+B2+FCC+σ	−	1069±14 (compressive)	−	17±2	[78]
	AN (950 °C, 6 T field)	BCC+FCC+σ	−	1057±12 (compressive)	−	22±1	
	AN (1200 °C, 0 T field)	BCC+B2	−	1254±13 (compressive)	−	21±2	
	AN (1200 °C, 6 T field)	BCC+FCC+σ	−	1231±73 (compressive)	−	26±4	
$Al_{0.5}CrCuFeNi_2$	AC	FCC	−	363 (tensile)	500	16.1	[79]
	AN (700 °C, 24 h)	BCC+FCC+$L1_2$	−	630 (tensile)	922	4.2	
	AN (900 °C, 24 h)	BCC+FCC+$L1_2$	−	704 (tensile)	1088	5.6	
	AN (1100 °C, 24 h)	FCC+$L1_2$	−	360 (tensile)	639	3.4	
$Al_{0.5}CoCrFeNi$	AC	BCC+FCC	−	355 (tensile)	714	41.6	[80]
	AN (650 °C, 8 h)	BCC+FCC+B2	−	834 (tensile)	1220	25	
$Al_{0.5}CoCrCuFeNi$	AN	−	−	656 (tensile)	796	29	[81]
	As-rolled	FCC+Cu-rich	3.913	1296 (tensile)	1406	6	
$Al_{0.3}CoCrFeNi$	AC	FCC	−	194 (compressive)	−	−	[82]
$Al_{0.6}CoCrFeNi$	AC	BCC+FCC	−	336 (compressive)	−	−	
$Al_{0.9}CoCrFeNi$	AC	BCC+B2	−	1342 (compressive)	−	−	
$Al_8Co_{17}Cr_{17}Cu_8Fe_{17}Ni_{33}$ (RT)	AC	FCC+$L1_2$	−	357(tensile)	456	9.0	[83]
	AN (700 °C, 5 h)	FCC+Cr-rich	−	365 (tensile)	365	0.1	
	AN (1150 °C, 5 h)	FCC+$L1_2$	−	215 (tensile)	489	39.0	
$Al_8Co_{17}Cr_{17}Cu_8Fe_{17}Ni_{33}$ (500 °C)	AC	−	−	315±12 (tensile)	334±1.0	0.7±0.3	[83]
	AN (700 °C, 5 h)	−	−	310±2.0 (tensile)	310±2.0	<0.02	
	AN (1150 °C, 5 h)	−	−	215±11 (tensile)	248±10	6.0±3.0	
$Al_{0.3}CoCrFeNi$	CR+SA (1150 °C, 60 min)	−	−	159±22 (tensile)	410±42	65±3	[84]
	CR+SA (1150 °C, 5 min)	−	−	220±20 (tensile)	550±35	60±4	
	CR+SA (1150 °C, 60 min) + AG (700 °C, 50 h)	−	−	215±16 (tensile)	520±21	43±6	
	CR+SA (1150 °C, 60 min) + AG (550 °C, 150 h)	−	−	285±14 (tensile)	540±43	55±12	
	CR+SA (1150 °C, 2 min)	−	−	263±32 (tensile)	589±51	60±7	
	CR+SA (1150 °C, 2 min) + AG (620 °C, 50 h)	−	−	490±22 (tensile)	840±24	45±8	

To be continued

Continued

Alloy	Processing method	Structure	Hardness/GPa	Yield strength/MPa	Ultimate tensile strength/MPa	Elongation/%	Ref.
$Al_{0.45}CoCrFeNiTi_x$ (x=0)	–	BCC + FCC	–	376 (tensile)	–	43	[85]
$Al_{0.45}CoCrFeNiTi_x$ (x=0.25)	–	BCC + FCC + $L2_1$	–	619 (tensile)	–	2.7	
$Al_{0.45}CoCrFeNiTi_x$ (x=0.5)	–	BCC + FCC + $L2_1$	–	694 (tensile)	–	0.19	
$Al_{65}Cu_{10}Mg_{10}Si_{10}Zn_5$	High-pressure die-casting	–	2.46	529 (compressive)	165	0.2	[86]
$Al_{14}Co_{41}Cr_{15}Fe_{10}Ni_{20}$	AC+HM (1200 °C, 20 h)	FCC + B2	–	523.5 (tensile)	977.5	17	[87]
	AC+AG (850 °C, 20 h)	–	–	574.5 (tensile)	890	8.25	
$AlCoCrFeNiTa_x$ (x=0)	AC	BCC + B2	4.88	–	–	–	[88]
	AC+Laser melting	–	5.31	–	–	–	
$AlCoCrFeNiTa_x$ (x=1)	AC	–	5.53	–	–	–	[88]
	AC+Laser melting	–	6.056	–	–	–	
$AlCoCrFeNiTa_x$ (x=3)	AC	–	6.25	–	–	–	[88]
	AC+Laser melting	–	6.99	–	–	–	
$Cr_{15}Fe_{20}Co_{35}Ni_{20}Mo_{10}$	AN (800 °C, 1 h) + AC	–	–	1311 (tensile)	1410	12.1	[89]
CrMnFeNiCu	AC	BCC+ FCC	–	~580 (tensile)	~1000	~27.9	[90]
	AN (900 °C, 24 h) + AC	FCC+ BCC+σ	–	547 (tensile)	657	~2.3	
	AN (950 °C, 24 h) + AC	FCC+ BCC+σ	–	549 (tensile)	598	~1.9	
$Fe_{28.2}Ni_{18.8}Mn_{32.9}Al_{14.1}Cr_6$	AC	FCC+B2	–	679±25 (tensile)	931 ± 3	17.8±0.2	[91]
	CR	FCC+B2	–	1422±35 (tensile)	1521 ± 33	2.3±0.3	
	CR+AN (1000 °C, 1 h)	FCC+B2	–	599±22 (tensile)	868 ± 10	19.5±1.4	
$(Fe_{50}Mn_{30}Co_{10}Cr_{10})_{100-x}Si_x$ (x=0)	Laser melting	FCC+HCP	2.324	325 (tensile)	741	27.7	[92]
$(Fe_{50}Mn_{30}Co_{10}Cr_{10})_{100-x}Si_x$ (x=4)	Laser melting	FCC+HCP	–	299 (tensile)	749	34.3	
$(Fe_{50}Mn_{30}Co_{10}Cr_{10})_{100-x}Si_x$ (x=8)	Laser melting	FCC+HCP	–	312 (tensile)	831	27.4	
$(Fe_{50}Mn_{30}Co_{10}Cr_{10})_{100-x}Si_x$ (x=12)	Laser melting	FCC+HCP	3.03	309 (tensile)	866	25.8	

To be continued

Continued

Alloy	Processing method	Structure	Hardness/GPa	Yield strength/MPa	Ultimate tensile strength/MPa	Elongation/%	Ref.
$Fe_{33}Co_{28}Ni_{28}Ta_5Al_6$	Laser melting (800 W)	BCC+FCC	−	1380 (tensile)	1550	5.8−6.2	[93]
	Laser melting (1000 W)	BCC+FCC	−	1340 (tensile)	1395	5.7−6.3	
	Laser melting (1200 W)	BCC+FCC	−	1250 (tensile)	1336	3.9−4.4	
	Laser melting (1400 W)	BCC+FCC	−	1225 (tensile)	1250	5.4−6.2	
$Ti_3Zr_{1.5}NbV_x$ (x=0)	AM	BCC	1.96	505.4 (tensile)	507.9	16.0	[94]
$Ti_3Zr_{1.5}NbV_x$ (x=1)	AM	BCC	2.48	707.6 (tensile)	712.1	9.8	
$Ti_3Zr_{1.5}NbV_x$ (x=2)	AM	BCC	2.918	974.0 (tensile)	984.2	6.3	
$UNbTiHf_{0.5}Mo_{0.5}$	AM	BCC	−	975 (compressive)	1673	37.8	[95]
$UNbTiHf_{0.3}Mo_{0.7}$	AM	Dual BCC	−	1145 (compressive)	1451	6.2	
$UNbTiHf_{0.1}Mo_{0.9}$	AM	Dual BCC	−	988 (compressive)	1360	4.2	

AC−Casting; CR−Cold rolling; SA−Solution treatment; AN−Annealing; AG−Aging; AC−Air cooling; WQ−Water quenching; MA−Mechanical alloying; SPS−Spark plasma sintering; PBFAM−Powder bed fusion additive manufacturing; HM−Homogenization; AM−Arc melting

The CoCrFeMnNi HEAs was subjected to cold rolling and recrystallization to achieve uniform microstructures with three distinct grain sizes of 4.4, 50 and 155 μm [98]. As illustrated in Figs. 7(a, b), as the grain size decreases, both the yield strength and ultimate tensile strength exhibit an increase. Furthermore, as the temperature decreases, the impact of grain refinement on the strengthening becomes more pronounced. The grain-refined (174.1 nm) $FeCrNiAlTi_{0.2}$ HEA exhibits excellent compressive strength (2745 MPa), yield strength (1877 MPa) and exceptional plastic strain (26.6%) [99]. GIGAX et al [100] prepared ultra-fine-grained CrFeMnNi HEAs by large-strain machining (LSM). As depicted in Figs. 7(c−f), EBSD images of CrFeMnNi HEA prepared under three different LSM conditions are presented. The microstructural analysis revealed the presence of ultra-fine grains across all conditions, with varying degrees of homogeneity. Its ultimate tensile strength also increased from the original 0.45 GPa to 0.73, 0.79, and 0.81 GPa, respectively.

The $V_{10}Cr_{15}Mn_5Fe_{35}Co_{10}Ni_{25}$ HEA exhibits varying grain sizes under different annealing treatments [101], as depicted in Figs. 7(g−k). At a temperature of 900 °C, annealing for 10 min resulted in the formation of fine grains (8.7 μm), while annealing at 1100 °C for 6 h yielded an average grain size of 82.7 μm. Correspondingly, the yield strength of the fine-grained sample (~401 MPa) is approximately twice that of the coarse-grained sample (~212 MPa).

It has been suggested that incorporating 0.19 wt.% of boron in the as-cast FeCoCrNiMn HEA can significantly refine its grain size [102]. By comparing Figs. 7(l, m), it can be seen that FeCoCrNiMn HEA with the addition of 0.19 wt.% B exhibits finer grains. According to the calculated results, the excess Gibbs free energy of Cr and B elements is the most negative, indicating that Cr and B elements are the most likely to aggregate together and form Cr_2B intermetallic compounds [102]. In addition, the melting point of the Cr_2B phase is about 2143 K, which is higher than that of the HEA (1603 K). Therefore, the Cr_2B phase formed before the HEA solidified during the metallurgical process [102]. As a result, the Cr_2B phase can act as an effective nucleating site to refine grains in FeCoCrNiMn HEA. Concurrently, boron atoms can divide the grain boundaries to hinder the grain growth, which can play a role in grain refinement [103].

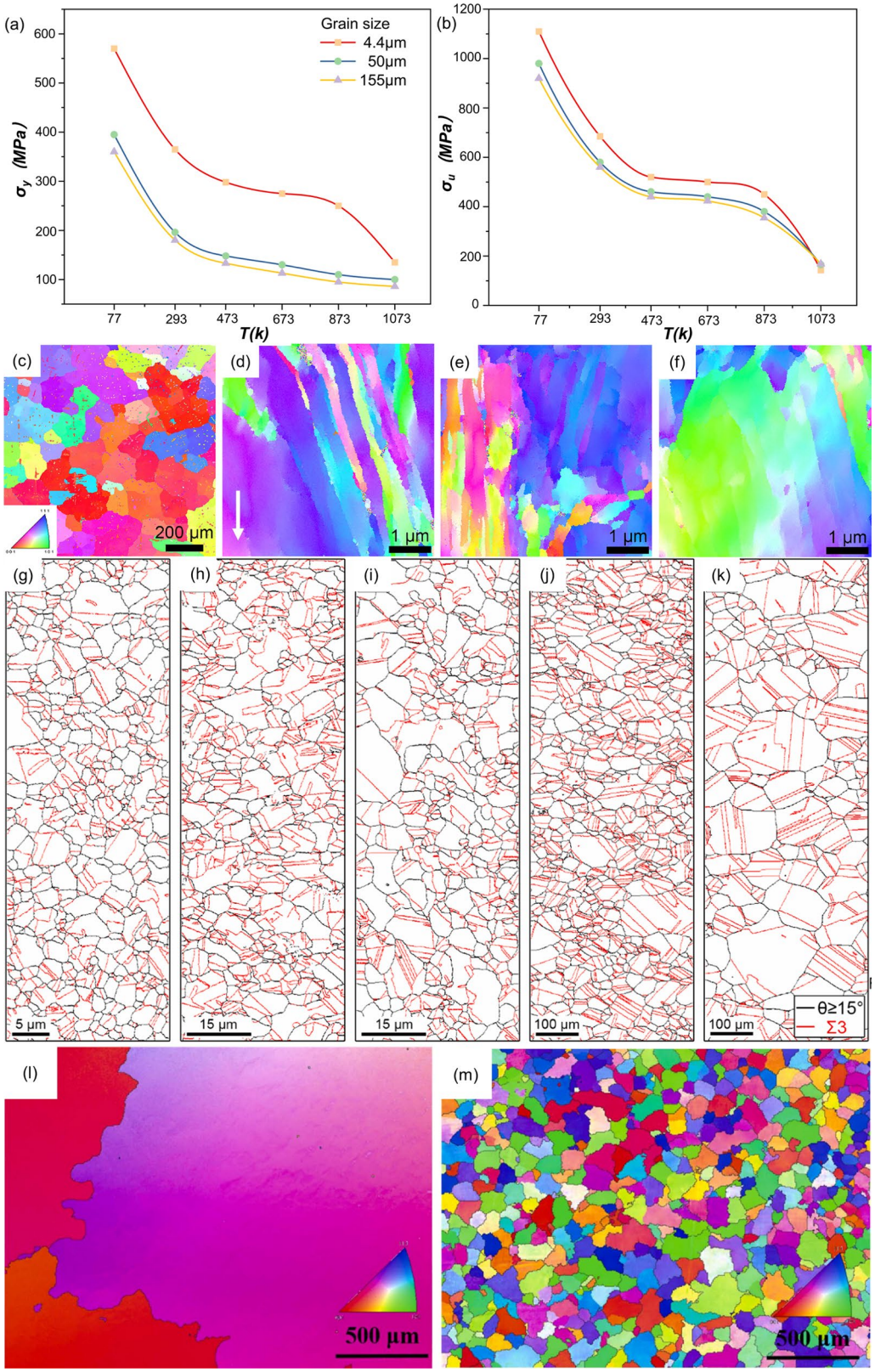

Fig. 7 0.2% offset yield stress (σ_y) (a) and ultimate tensile strength (σ_u) (b) for CoCrFeMnNi alloy [98]; EBSD pole figure map of base material (c) and SEM micrographs of HEA-1 subject to LSM conditions of 1 m/s and 0° (d), 1.7 m/s and 0°(e), and 1 m/s and −10°(f) (The machining direction for all LSM conditions is labelled in (d) with a white arrow) [100]; EBSD grain boundary maps of $V_{10}Cr_{15}Mn_5Fe_{35}Co_{10}Ni_{25}$ HEA after annealing under different conditions of 900 °C, 10 min (g), 900 °C, 30 min (h), 900 °C, 60 min (i), 1000 °C, 60 min (j) and 1100 °C, 360 min (k), (Black and red lines are high-angle grain boundaries and annealing twin boundaries, respectively) [101]; EBSD maps of equiaxed zone of HEA without B adding (l) and with 0.19 wt.% B adding (m) [102]

5.2 Solid solution strengthening

The introduction of solute atoms into a crystal lattice results in lattice distortion, necessitating a higher shear stress to facilitate the movement of dislocations within the lattice. The enhancement in the mechanical strength of a solid-solution alloy attributed to the presence of solute atoms is referred to as solid solution strengthening [96], which can be divide into interstitial solid solution strengthening and substitutional solid solution strengthening.

5.2.1 Interstitial solid solution strengthening

It was suggested that the addition of O could cause the formation of ordered oxygen complexes (OOCs) in TiZrHfNb HEA [104]. The $(TiZrHfNb)_{98}O_2$ HEA (O-2 HEA) demonstrated exceptional yield strength ((1.11±0.03) GPa) and outstanding elongation ((27.66±1.13)%). The interstitial solid solution strengthening in the O-2 HEA is demonstrated in Figs. 8(a−e). In the initial phases of plastic deformation, planar slip remains dominant (Fig. 8(b)). However, when dislocations come into contact with the highly distorted, interstitial-enriched OOCs, the pinning effects of these obstacles promote cross-slip (Fig. 8(c)), leading to significant multiplication of dislocations (Fig. 8(d)). As a result, an increasing number of dislocations are pinned by OOC, and dipolar walls begin to appear as the strain level rises (Fig. 8(e)). This phenomenon enhances the process of work hardening and postpones the initiation of necking, ultimately resulting in increased ductility. Throughout the process of deformation, these OOCs engage with dislocations by means of impeding their movement and facilitating the occurrence of dislocation double cross-slip (Fig. 8(f)).

WANG et al [105] systematically studied the interstitial solid solution strengthening of HEAs by adding different contents of C elements to the $Fe_{40.4}Ni_{11.3}Mn_{34.8}Al_{7.5}Cr_6$ HEA. Figure 8(g) illustrates the uniform distribution of all elements. The results demonstrated that the yield strength and

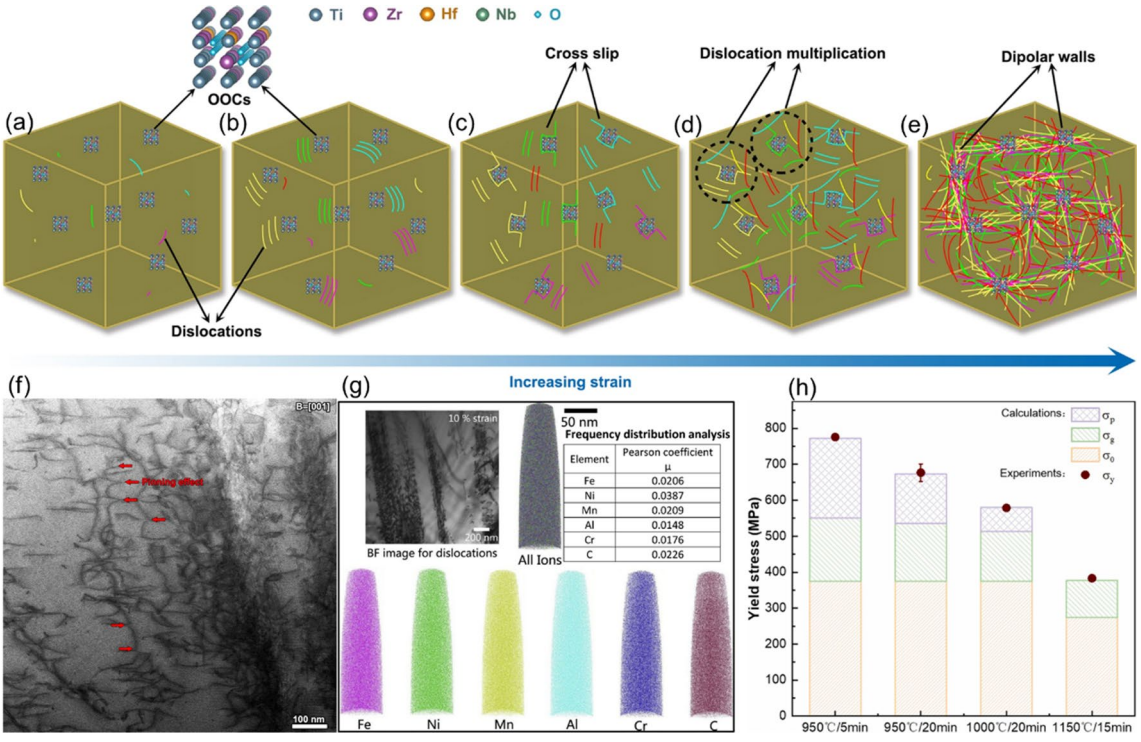

Fig. 8 Schematic diagram illustrating plastic deformation mechanism in oxygen-rich alloy variant O-2 HEA (a−e) [104]; Aberration-corrected STEM observation of O-2 HEA after being prestrained to 8% (*B* is the beam direction; The red arrows indicate the distinct dislocation pinning effect, which suppresses dislocation motion substantially during deformation) (f) [104]; Atom probe tomography (APT) elemental maps and frequency distribution analysis of 1.1 at.% carbon-doped $Fe_{40.4}Ni_{11.3}Mn_{34.8}Al_{7.5}Cr_6$ HEA after 10% strain (The inserted BF TEM image shows the pile-up of dislocations) (g) [105]; Theoretical calculation results of multiple strengthening effects for (950 °C, 5 min)-annealed, (950 °C, 20 min)-annealed, (1000 °C, 20 min)-annealed and (1150 °C, 15 min)-annealed dual-interstitial HEA samples (The red dots indicate the yield stress value attained from experiments) (h) [106]

final tensile strength increase with the increase of C element content, and the plasticity also increases to some extent. It has been proposed that the introduction of carbon results in a lattice strain of 0.78/at.% and a corresponding increase in yield strength of 184 MPa/at.%. $Fe_{40.4}Ni_{11.3}Mn_{34.8}Al_{7.5}Cr_6$ HEA doped with C demonstrates a notable increase in strain hardening rate. This phenomenon can effectively postpone necking and consequently stabilize plastic deformation, thereby contributing to the enhancement of plasticity.

5.2.2 Substitutional solid solution strengthening

HU et al [106] used dual interstitial alloying C and N to improve the strength−ductility synergy of the FCC CoCrFeMnNi HEA, which demonstrates superior mechanical properties, including high yield strength (772 MPa), high ultimate tensile strength (1178 MPa), and remarkable elongation (34%). In order to quantitatively analyze the various factors contributing to the strength of the HEA samples, several equations are utilized to estimate the yield strength:

$$\sigma_y=\sigma_0+\sigma_g+\sigma_p \quad (13)$$

where the value of σ_0 is determined by the combined effects of lattice friction stress (σ_f) and solid solution strengthening (σ_s). σ_g and σ_p are strengthening contributions from the grain boundaries and precipitates, respectively. Furthermore, the CoCrFeMnNi HEA exhibits a calculated value of σ_0 at 274 MPa, indicating a substantial/interstitial strengthening effect from solid solution of C and N [106]. For the (1150 °C, 15 min)-annealed dual interstitial HEA sample, the contribution of σ_0 to the total yield strength was ~73% (Fig. 8(h)).

5.3 Second phase strengthening

From the source of the second phase, the second phase strengthening is divided into dispersion strengthening and precipitation strengthening. Dispersion strengthening refers to the process of strengthening an alloy by introducing a second phase particle through the addition of an alloying element [107]. Precipitation strengthening is also known as coherent precipitation strengthening or age hardening. Coherent precipitates are produced by heat treatment or other means, which hinder the dislocation movement and thus improve the mechanical properties of the material [90,101].

5.3.1 Precipitation strengthening

It was suggested that with appropriate thermo-mechanical treatment, small amounts of Ti and Al element addition can produce fine dispersions of $L1_2$ $Ni_3(Ti,Al)$-type γ' coherent nanoprecipitation in FCC FeCoNiCr HEA [108]. As depicted in Figs. 9(a, b), the FeCoNiCr HEAs produced through the P1 and P2 treatments contain small precipitates that are expected to increase the strength through the dislocation by-pass mechanism (Orwan-type) or the particle shear mechanism. The P1 HEA consists of two different sizes of precipitate morphologies: the nanoprecipites in Region I are less than 40 nm, while the particles in Region II are coarse of more than 100 nm. P1 HEA has high yield strength (645 MPa) and excellent elongation (39%). The alloy produced through P2 process exhibits a yield strength up to 1 GPa, while also maintaining an unexpected elongation of approximately 17%.

The $Al_{0.2}CrFeCoNi_2Cu_{0.2}$ HEA with $L1_2$ $(Ni,Cu)_3Al$ nanoprecipitates exhibits superior yield strength (719 MPa) and ultimate tensile strength (1048 MPa) without sacrificing plasticity (30.4%) [109]. The formation of the $L1_2$ $(Ni,Cu)_3Al$ nano-precipitates is attributed to the negative mixing enthalpy of Al, Cu, and Ni elements [110,111]. It has been proposed that the emergence of $L1_2$ nanoprecipitates leads to an increase of 259 MPa in yield strength and 316 MPa in ultimate tensile strength. Furthermore, due to the presence of $L1_2$ nanoprecipitates, the dislocation configuration becomes a planar dislocation slip consisting of crystallographic slip bands (Fig. 9(d)), ultimately leading to a significant increase in work hardening capability without sacrificing ductility.

It was suggested that the dispersion of nano-sized and semicoherent precipitates driven by shear bands results in notable strengthening effects in $Al_{0.2}CoNiV$ HEA [112]. As the annealing temperature increases, the precipitation of $L2_1$ phase in $Al_{0.2}CoNiV$ begins to occur at grain boundaries or triple junctions during the process of recrystallization. The EBSD images of the $Al_{0.2}CoNiV$ alloy annealed at various temperatures are depicted in Figs. 9(e−g). Annealing at 850 °C resulted in the emergence of $L2_1$ precipitates, leading to the exceptional strength (1587 MPa) and ductility (26.7%) of the $Al_{0.2}CoNiV$ alloy.

A new $Ni_{35}(CoFe)_{55}V_5Nb_5$ HEA with an excellent ultimate tensile strength (1302 MPa) and

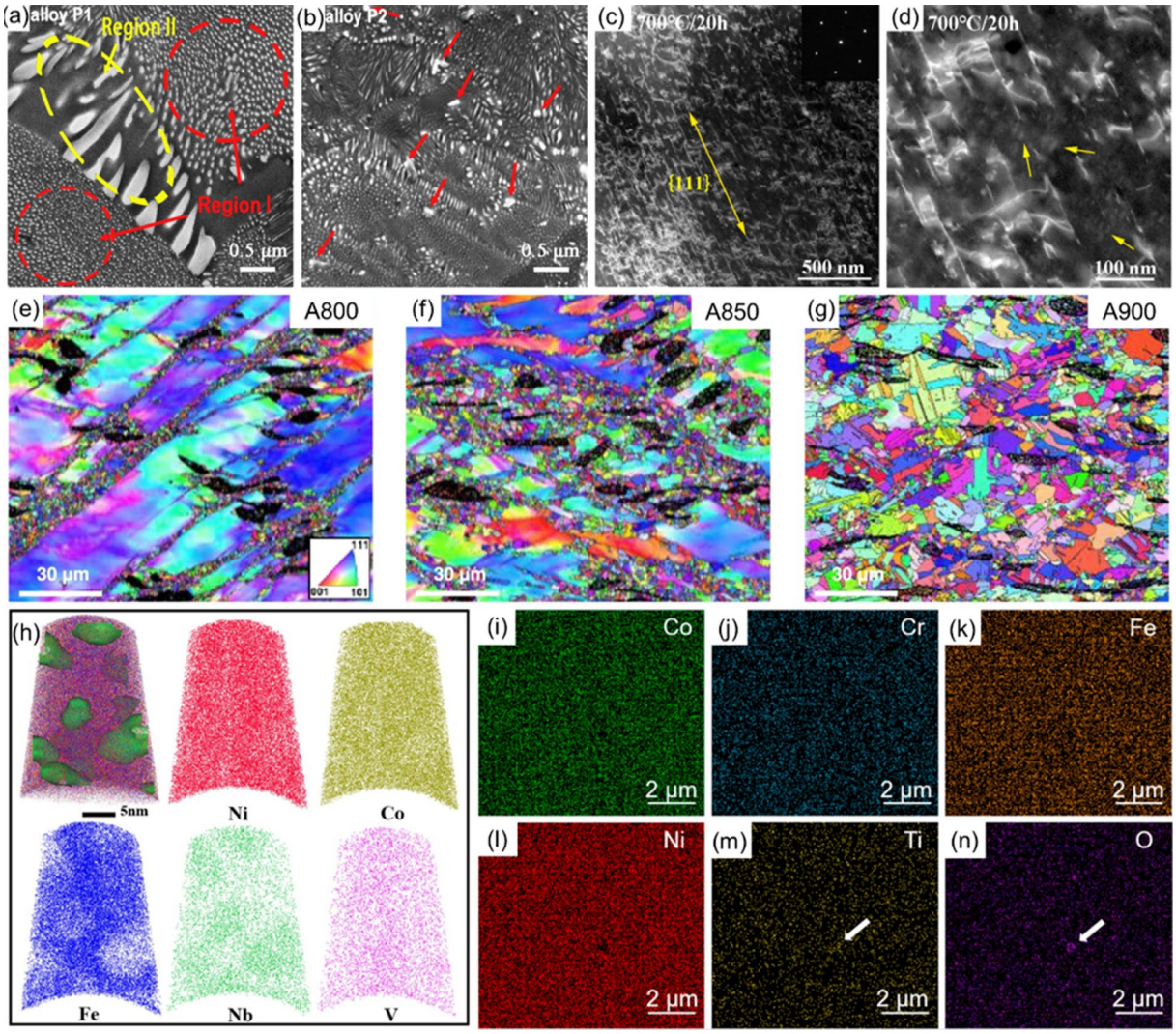

Fig. 9 Enlarged views of precipitate morphology for P1 (a) and P2 (b) alloys, respectively; STEM HAADF images showing dislocation patterning developed during tensile straining for $L1_2$ $(Ni,Cu)_3Al$ nanoprecipitates alloy (c) and enlarged view showing split of precipitates caused by dislocation shearing (d) [108]; EBSD maps of FCC $Al_{0.2}CoNiV$ alloy (e−g) [112]; APT maps with Ni, Co, Fe, Nb, and V, and iso-concentration interface plotted at 10 at.% Nb of $Ni_{35}(CoFe)_{55}V_5Nb_5$ HEA (h) [113]; corresponding EDX elemental maps of $Ni_2CoCrFeTi_{0.2}$ HEA (i−n) [116]

elongation (~50%) synergy was developed by introducing a novel bifunction $L1_2$-Ni_3Nb nano-precipitate [113]. The new precipitate has a dual function. The concentrations of Ni, Co, Fe, Nb, and V in the precipitates and matrix were examined using APT, as illustrated in Fig. 9(h). On the one hand, the $L1_2$-$(Ni_{24}Co_{18}Fe_6)_3(Nb_{10}V_4Fe_2)$ nano-precipitates have high anti-phase boundary energy, and thereby the strength is significantly improved by precipitation strengthening. On the other hand, the precipitate reduces the stacking fault exergy (SFE) of the alloy matrix, leading to the formation of stacking fault networks and Lorner−Cottrell (LC) locks during deformation.

5.3.2 Dispersion strengthening

Due to its elevated hardness and resistance to high temperatures [114], Y_2O_3 is frequently employed as a dispersoid in oxide dispersion strengthening alloys. $Al_{0.3}CoCrFeMnNi$+3%Y_2O_3 HEAs with nano-dispersions by adding 3 vol.% Y_2O_3 were prepared [115]. The yield strength of this HEA increased from 979 to 1759 MPa at the beginning, while maintaining reasonable ductility (19.8%). CHENG et al [116] achieved synergistic improvements in strength (1070 MPa) and ductility (11.6%) by designing the heterogeneous grain structures and dispersing oxide nanoparticles in $Ni_2CoCrFeTi_{0.2}$ HEA. The FCC matrix displayed an

even dispersion of its constituent elements, while the oxide particles appeared to have a higher concentration of Ti and O elements (Figs. 9(i−n)). Through quantitative analysis, it was suggested that oxide dispersion strengthening is one of the important reasons for improving the mechanical properties of $Ni_2CoCrFeTi_{0.2}$. Based on prior research, it has been found that oxide nanoparticles have the potential to impede the migration of grain boundaries, thereby contributing to the prevention of grain coarsening at elevated temperatures [117,118].

5.4 Short-range order strengthening

Short-range order (SRO) refers to ordering at a distance comparable to the distance among atoms. Since the interaction energy between some atomic pairs are lower than others, these specific pair configurations are more energetically favorable. Thereby the specific pair with lower interaction energy are more than the random case [119]. SRO strengthening of HEAs is a new strengthening method proposed in recent years, but remarkable achievements have been made in achieving the strength and plasticity of HEAs.

Many are scholars systematically investigated a CoCuFeNiPb HEA by using Monte Carlo method, molecular dynamic simulation, and density-functional theory calculation [120]. It is suggested that SRO causes the formation of pseudo-composite microstructures of BCCP (body-center-cubic-preferred), IND (indifferent clusters), FCCP (face-center-cubic-preferred) structures and IND plays the role of matrix. FCCP acts as a hard filler to improve the strength while BCCP as a soft filler to enhance the plasticity. Therefore, the prepared HEA exhibits excellent comprehensive mechanical properties. Figures 10(a−e) illustrate a strategy for designing HEAs that enhance both strength and ductility by SRO. Figure 10(a) illustrates required

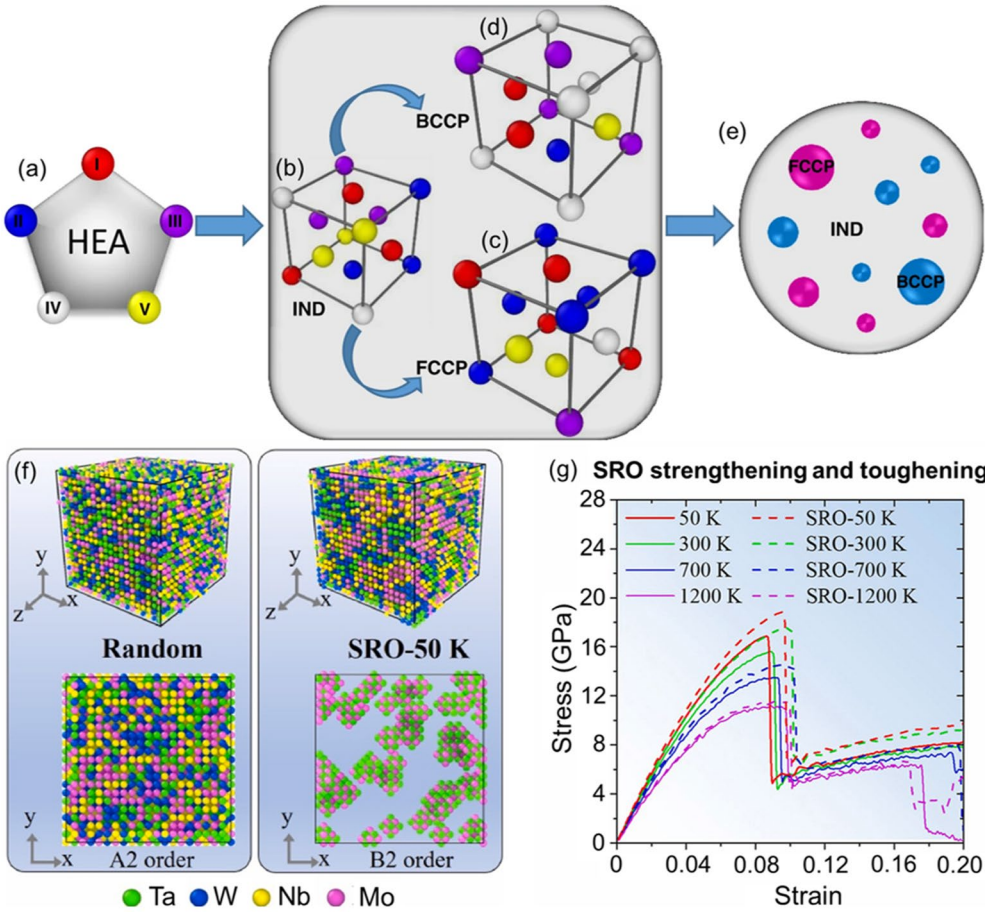

Fig. 10 Design of HEA with five elements (I, II, III, IV, and V) (a), formations of IND (b), FCCP (c), and BCCP (d) clusters via short-range ordering and IND clusters serving as matrix with FCCP clusters serving as hard fillers to enhance strength and BCCP clusters acting as soft fillers to increase ductility (e) [120]; Atomic configurations with random distribution and SRO at 50 K (For the B2 order snapshot, the A2 (BCC) atoms are not shown) (f); Stress−strain curves of structures with random distribution and SRO at different temperatures (g) [121]

conditions to form such a composite microstructure with five elements. First of all, the five different elements prefer to form a stable FCC structure in the solid-solution phase (Fig. 10(b)). Secondly, the stable FCCP domains are able to form via SRO (Fig. 10(d)). Then, the BCCP domains can also be formed, and the FCC structure is metastable in BCCP domains (Fig. 10(c)). Finally, structures with FCCP and BCCP are formed in the IND matrix.

It was suggested that the presence of SRO can enhance both strength and toughness of equiatomic NbMoTaW RHEA over a wide temperature range even at very fast strain rates [121]. According to Gibbs free energy, when the temperature is lower, entropy has less effect on free energy than enthalpy. Therefore, it is more energetically desirable to cause the formation of SRO by reducing the enthalpy at low temperatures. So, the degree of SRO is higher at low temperatures, and the enhancement is larger. The atomic arrangements are depicted in Fig. 10(f). Figure 10(g) shows the stress-strain curve of a structure with random distributions and SROs at different temperatures. The increased strength of the SRO RHEA is associated with its higher twin stacking fault energy, resulting in elevated yield strength. Similarly, the enhanced toughness of the SRO RHEA is linked to its higher twin boundary migration energy, resulting in increased flow stress.

5.5 TRIP strengthening and toughening

In the case of conventional alloys, the conversion of residual austenite to martensite often results in significant work hardening, which improves the strength and plasticity of the alloy simultaneously [122,123]. This phenomenon is referred to as transformation-induced plasticity (TRIP) effect.

The $Cr_{20}Mn_6Fe_{34}Co_{34}Ni_6$ HEA (DP-HEA) exhibits excellent tensile strength at room temperature (~1 GPa) and outstanding tensile plasticity (~60%), which is significantly higher than CrMnFeCoNi Cantor HEA (Fig. 11(a)) [124]. This is caused by the gradual increase in the proportion of the stronger HCP phase formed at the stacking fault network in the FCC phase during plastic deformation, which becomes the primary source of strain hardening and consequently enhances the strength. Figures 11(b, c) demonstrate a comparison of the microstructures of DP-HEA and Cantor alloys. The inset in Fig. 11(c) is the phase diagram of DP-HEA, where the red color represents the FCC austenite phase, and the green color represents the HCP phase. Later, the microstructure and mechanical properties of a TRIP HEA ($Cr_{20}Mn_{24}Fe_{30}Co_{20}Ni_6$, at.%) after cold-rolling and annealing were systematically investigated [125]. The enlarged view in Fig. 11(e) from the rectangle region in Fig. 11(d) highlights the presence of nano-sized σ precipitates, as indicated by the white arrows. Although the nano-precipitates play a substantial role in enhancing strength of $Cr_{20}Mn_{24}Fe_{30}Co_{20}Ni_6$, they also result in the propagation of micro-voids and premature fracture during deformation.

$Ti_{35}Zr_{27.5}Hf_{27.5}Nb_5Ta_5$, $Ti_{38}Zr_{25}Hf_{25}Ta_{10}Sn_2$ and $Ti_{38}Zr_{25}Hf_{25}Ta_7Sn$ exhibited surprisingly high strain hardening and ductility [126]. Prior studies have demonstrated that the TRIP effect is commonly responsible for the attainment of high strain-hardening [127,128]. As illustrated in Figs. 11(i−k), the microstructural examinations presented the compelling evidence of the manifestation of the TRIP effect during the tensile deformation of all three alloys. Initially, the limited slip system of the HCP phase may result in the transformed HCP (α') phase exhibiting greater strength than the matrix BCC (β) phase, consequently enhancing the material's strength. Furthermore, the transformed α' gives rise to a separate phase boundary in comparison to the original β matrix. As a result, the occurrence of phase boundary resulting from the formation of α' serves to enhance the effective β grain size and reduce the average distance for the dislocation slip. Thereby, the TRIP effect is conducive to the combination of high strength and ductility.

5.6 MBIP strengthening and toughening

Microband induced plasticity (MBIP) effect plays a significant role as a crucial mechanism for ductility, which generates strain hardening effects comparable to those induced by TWIP and TRIP effect. Microbands are formed as a result of dislocation slip, leading to the subdivision and refinement of grains, thereby enhancing the mechanical properties of the material [129].

A new $CoCrNi_2(Al_{0.2}Nb_{0.2})$ $L1_2$-strengthened

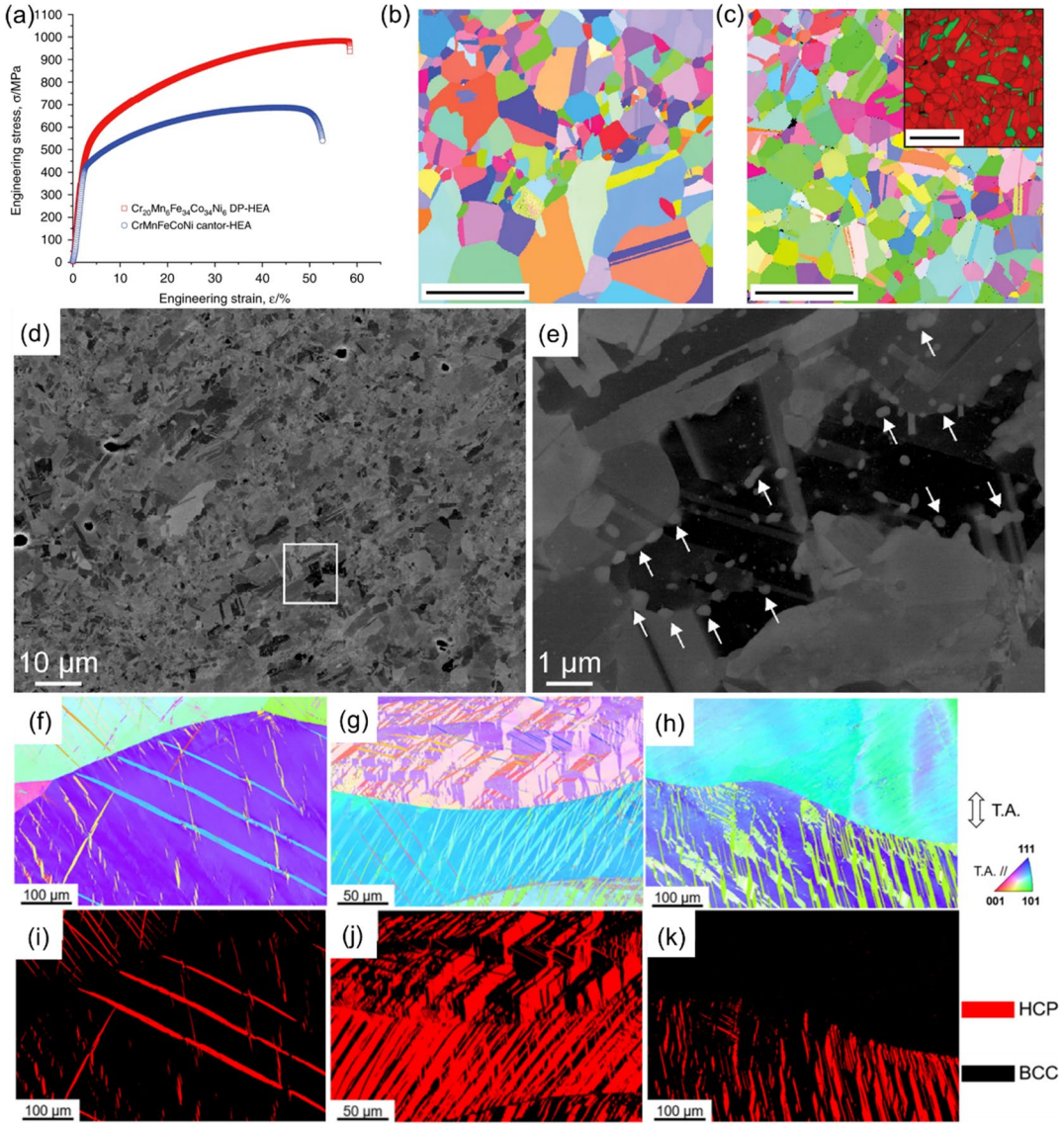

Fig. 11 Engineering uniaxial tensile stress–strain curves for DP-HEA compared to those of CrMnFeCoNi Cantor HEA (a); Corresponding EBSD maps of microstructures of Cantor alloy (b) and DP-HEA (c) [124]; Low magnification overview BSE (d) and enlarged view (e) showing nano-sized σ precipitates [125]; EBSD IPF maps of $Ti_{35}Zr_{27.5}Hf_{27.5}Nb_5Ta_5$ (f), $Ti_{38}Zr_{25}Hf_{25}Ta_{10}Sn_2$ (g), and $Ti_{38}Zr_{25}Hf_{25}Ta_7Sn_5$ (h) (Colors of the microstructures indicate crystallographic orientations parallel to the tensile axis according to the key stereographic triangle), and phase maps of $Ti_{35}Zr_{27.5}Hf_{27.5}Nb_5Ta_5$ (i), $Ti_{38}Zr_{25}Hf_{25}Ta_{10}Sn_2$ (j), and $Ti_{38}Zr_{25}Hf_{25}Ta_7Sn_5$ (k) (HCP and BCC phases are shown in red and black colors, respectively; Tensile axis is parallel to the vertical axis of microstructures) [126]

HEA was prepared by thermodynamic approach, which exhibits excellent yield strength (1.15 GPa), tensile strengths (1.6 GPa) and ductility (~33%) [129]. As shown in Fig. 12(b), when the strain was increased to 18%, the appearance of microbands can be observed. When the strain was increased to 30%, the crossing of the microbands can be observed in TEM image (Fig. 12(c)). Figure 12(d) illustrates a schematic diagram of the evolution of the microstructure during deformation. It is suggested that the microbands are characterized by local high-density dislocation, which can be attributed to the strain localization during the deformation. In addition, due to the large size of Nb atoms, the frictional stress increases, which can hinder the formation of dislocation cells, thus, favorable for the development of microbands [105]. As a result, the presence of microband structures effectively enhances strain hardening and achieves excellent tensile ductility even at high strength levels.

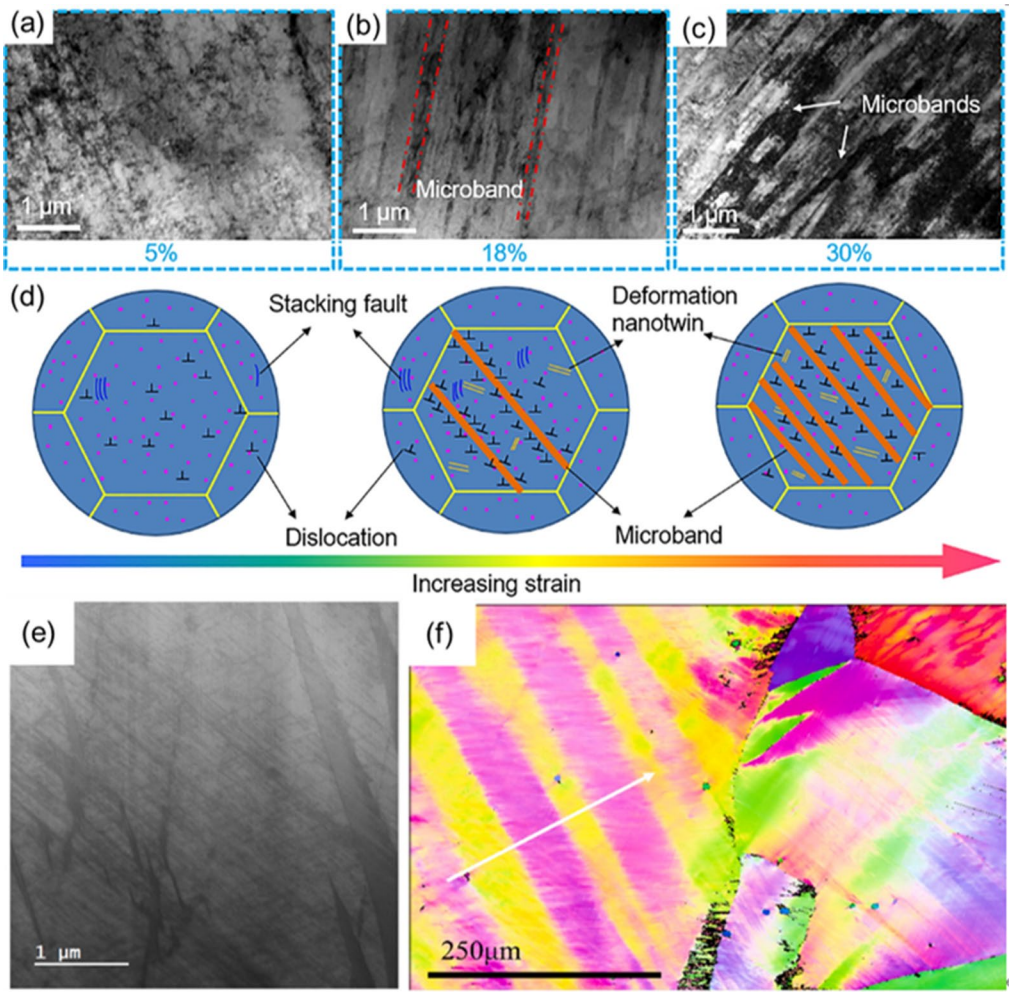

Fig. 12 Bright-field TEM images of alloy with varying strains of 5% (a), 18% (b), and 30% (c) and sample with strain of 30% revealing formation of microbands [129]; Schematic illustration of microstructure evolution during deformation (d) [129]; TEM bright-field micrographs displaying strong planar glide and intersecting microbands (e) and showing existence of deformation-induced microbands and corresponding misorientation profile (f) at compressive strain of 0.15 of HEA sample [130]

The non-equiatomic FeNiCoAlTaB HEA exhibits outstanding strength and remarkable work hardening ability [130]. As depicted in Fig. 12(e), when the compressive strain reaches 0.15, microbands consisting of a double-wall structure and strong planar slip on the slip plane can be observed, and they have a linear array of dislocation configurations. Hence, microbands possess the dual capacity to exhibit plasticity and facilitate the accumulation of dense dislocations, while also playing a crucial role in strain hardening by creating barriers that impede the movement of dislocations [131]. It is proposed that the formation of microbands can be attributed to two factors: non-equimolar FeNiCoAlTaB HEA has high SFE and coarse grains, which favors the formation of heterogeneous dislocation substructures [132]. In addition, the strong planar slip and linear arrangement of dislocations that occur during experiments are often considered to be the precursors of microbands [130].

6 Concluding remarks and outlook

This work provides an overview of the latest research progress in HEAs, focusing on phase structure prediction and mechanical properties. It specifically highlights the strengthening and toughening strategies of HEAs to maximize their application effectiveness. As depicted in Fig. 13, the utilization of HEAs across diverse domains, along with strategies for enhancing strength and

toughness, properties, and current areas of research focus are illustrated.

We conducted an analysis on the strengthening and toughening of HEAs through methods such as grain refinement, solid solution strengthening, second-phase strengthening, short-range ordered strengthening, TRIP, and MBIP. Solid solution strengthening results in work hardening, delaying the onset of necking and stabilizing plastic deformation, ultimately leading to enhanced ductility. The introduced second phase may act as an effective nucleating site to promote the formation of fine grains in HEAs, which can play a role in fine-grain strengthening. In addition, it is also possible to act as interstitial atoms, thereby hindering the dislocation movement and improving the strength of the alloy. Short-range orderly strengthening of HEAs is a novel strengthening method proposed in recent years. It is proposed that the degree of SRO is higher at low temperatures, leading to more significant strengthening effect. Furthermore, it is demonstrated that TRIP and MBIP are powerful means to achieve a balance between strength and ductility in HEAs.

The exceptional mechanical properties exhibited by HEAs are indicative of their potential to play a pivotal role in future engineering applications. LHEAs can take advantage of their light weight and high strength, making them suitable as raw materials for numerous components in automobiles, effectively reducing the overall weight of the vehicles. The excellent elevated-temperature mechanical properties exhibited by RHEAs are expected to fill the gap in the ultra-high-temperature field where nickel-based super-alloys fall short, making them the potential next-generation material for turbine blades in aerospace engines. HEAs possess notable attributes such as high wear resistance, corrosion resistance, and excellent biocompatibility, rendering them suitable for application in orthopedic implants and as implements in surgical operation. Due to its excellent castability, mechanical properties, and corrosion resistance, EHEAs have significant potential for application in the maritime and ocean engineering sectors. Future efforts should focus on enhancing the mechanical properties of EHEAs and conducting research on their microstructure in marine environments to expedite their utilization in the field of shipbuilding. Furthermore, HEAs are more stable and cost-effective compared to traditional catalytic materials, with higher catalytic efficiency, which also makes HEAs promising for significant impact in the field of catalysis. In

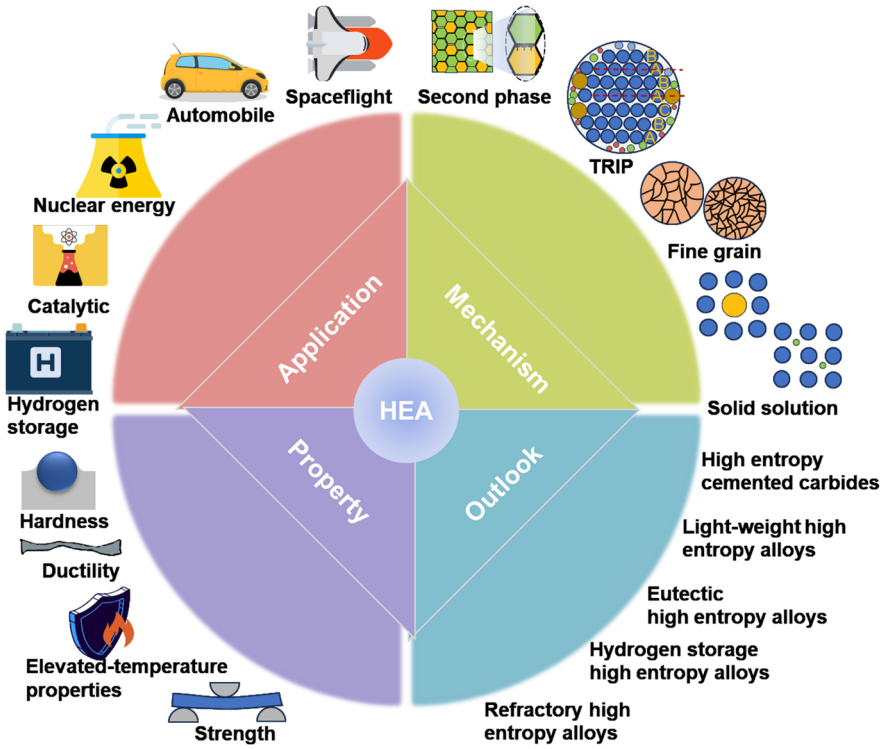

Fig. 13 Schematic diagram of strengthening and toughening, applications, properties, and development trends of HEAs

addition, HEAs also have great application prospects in the field of nuclear energy, hydrogen energy and other fields.

However, further research is needed to delve into the selection of components for HEAs and the mechanisms balancing strength and ductility. It is necessary to reduce the production cost of HEAs in order to promote their wider application. Eutectic high-entropy alloys, high-entropy cemented carbides and refractory high-entropy alloys are believed to have extremely broad application prospects in the field of engineering.

CRediT authorship contribution statement

Bin LI: Methodology, Formal analysis, Data curation, Writing − Original draft; **Jia-lin SUN:** Funding acquisition, Conceptualization, Supervision, Writing − Review & editing, Methodology; **Jun ZHAO:** Writing − Review & editing; **Xia-lun YUN:** Writing − Review & editing; **Quan-bin DU:** Writing − Review & editing.

Declaration of competing interest

The authors declare that they have no known competing financial interests or personal relationships that could have appeared to influence the work reported in this paper.

Acknowledgments

This work was supported by the National Natural Science Foundation of China (Nos. 52375451, 52005396), Shandong Provincial Natural Science Foundation, China (Nos. ZR2023YQ052, ZR2023ME087), Shandong Provincial Technological SME Innovation Capability Promotion Project, China (No. 2023TSGC0375), Young Taishan Scholars Program of Shandong Province, China (No. tsqn202306041), Guangdong Basic and Applied Basic Research Foundation, China (No. 2023A1515010044), Shandong Provincial Youth Innovation Team, China (No. 2022KJ038), Open Project of State Key Laboratory of Solid Lubrication, China (No. LSL-22-11), Young Talent Fund of University Association for Science and Technology in Shaanxi, China (No. 20210414), and Qilu Youth Scholar Project Funding of Shandong University, China.

References

[1] LI Zhi-ming, PRADEEP K G, DENG Yun, RAABE D, TASAN C C. Metastable high-entropy dual-phase alloys overcome the strength–ductility trade-off [J]. Nature, 2016, 534(7606): 227−230.

[2] LUO Kai-guang, WU Yu-ze, XIONG Han-qing, ZHANG Yun, KONG C, YU Hai-liang. Enhanced mechanical properties of aluminum matrix composites reinforced with high-entropy alloy particles via asymmetric cryorolling [J]. Transactions of Nonferrous Metals Society of China, 2023, 33(7): 1988−2000.

[3] ZHANG Yong, ZUO Ting-ting, TANG Zhi, GAO M C, DAHMEN K A, LIAW P K, LU Zhao-ping. Microstructures and properties of high-entropy alloys [J]. Progress in Materials Science, 2014, 61: 1−93.

[4] CHEN Shuai, LIU Ping, PEI Qing-xiang, YU Zhi-gen, AITKEN Z H, LI Wang-hui, WU Zhao-xuan, BANERJEE R, SROLOVITZ D J, LIAW P K, ZHANG Yong-wei. Ideal plasticity and shape memory of nanolamellar high-entropy alloys [J]. Science Advances, 2023, 9(41): 5817.

[5] TIAN Yu-sheng, ZHOU Wen-zhe, TAN Qing-biao, WU Ming-xu, QIAO Shen, ZHU Guo-liang, DONG An-ping, SHU Da, SUN Bao-de. A review of refractory high-entropy alloys [J]. Transactions of Nonferrous Metals Society of China, 2022, 32(11): 3487−3515.

[6] CAO Yuan-kui, LIU Yong, LIU Bin, ZHANG Wei-dong, WANG Jia-wen, DU Meng. Effects of Al and Mo on high temperature oxidation behavior of refractory high entropy alloys [J]. Transactions of Nonferrous Metals Society of China, 2019, 29(7): 1476−1483.

[7] REN Jin-tao, CHEN Lei, WANG Hao-yu, YUAN Zhong-hua. High-entropy alloys in electrocatalysis: From fundamentals to applications [J]. Chemical Society Reviews, 2023, 52(23): 8319−8373.

[8] ZHANG Zhou-ran, ARMSTRONG D E J, GRANT P S. The effects of irradiation on CrMnFeCoNi high-entropy alloy and its derivatives [J]. Progress in Materials Science, 2022, 123: 100807.

[9] TSAI K Y, TSAI M H, YEH J. W. Sluggish diffusion in Co−Cr−Fe−Mn−Ni high-entropy alloys [J]. Acta Materialia, 2013, 61: 4887−4897.

[10] VAIDYA M, TRUBEL S, MURTY B S, WILDE G, DIVINSKI S V. Ni tracer diffusion in CoCrFeNi and CoCrFeMnNi high entropy alloys [J]. Journal of Alloys and Compounds, 2016, 688: 994−1001.

[11] VAIDYA M, PRADEEP K G, MURTY B S, WILDE G, DIVINSKI S V. Radioactive isotopes reveal a non sluggish kinetics of grain boundary diffusion in high entropy alloys [J]. Scientific Reports, 2017, 7(1): 12293.

[12] VAIDYA M, PRADEEP K G, MURTY B S, WILDE G, DIVINSKI S V. Bulk tracer diffusion in CoCrFeNi and CoCrFeMnNi high entropy alloys [J]. Acta Materialia, 2018, 146: 211−224.

[13] ZHANG Chuan, ZHANG Fan, JIN Ke, BEI Hong-bin, CHEN Shuang-lin, CAO Wei-sheng, ZHU Jun, LV Du-chao. Understanding of the elemental diffusion behavior in concentrated solid solution alloys [J]. Journal of Phase Equilibria and Diffusion, 2017, 38(4): 434−444.

[14] GAERTNER D, ABRAHAMS K, KOTTKE J, ESIN V A, STEINBACH I, WILDE G, DIVINSKI S V. Concentration-dependent atomic mobilities in FCC CoCrFeMnNi high-entropy alloys [J]. Acta Materialia, 2019, 166: 357−370.

[15] KOTTKE J, LAURENT-BROCQ M, FAREED A, GAERTNER D, PERRIèRE L, ROGAL Ł, DIVINSKI S V, WILDE G. Tracer diffusion in the Ni−CoCrFeMn system:

Transition from a dilute solid solution to a high entropy alloy [J]. Scripta Materialia, 2019, 159: 94−98.

[16] YEH J W, CHEN S K, LIN S J, GAN J Y, CHIN T S, SHUN T T, TSAU C H, CHANG S Y. Nanostructured high-entropy alloys with multiple principal elements: Novel alloy design concepts and outcomes [J]. Advanced Engineering Materials, 2004, 6(5): 299−303.

[17] YEH J W. Recent progress in high-entropy alloys [J]. European Journal of Control, 2006, 31: 633−648.

[18] MIRACLE D B, MILLER J D, SENKOV O N, WOODWARD C, UCHIC M D, TILEY J. Exploration and development of high entropy alloys for structural applications [J]. Entropy, 2014, 16: 494−525.

[19] CHEN Peng-cheng, LIU Xiao-long, HEDRICK J L, XIE Zhuang, WANG Shun-zhi, LIN Qing-yuan, HERSAM M C, DRAVID V P, MIRKIN C A. Polyelemental nanoparticle libraries [J]. Science, 2016, 352(6293): 1565−1569.

[20] YAO Yong-gang, HUANG Zhen-nan, XIE Peng-fei, LACEY S D, JACOB R J, XIE Hua, CHEN Feng-juan, NIE An-min, PU Tian-cheng, REHWOLDT M, YU Dai-wei, ZACHARIAH M R, WANG Chao, SHAHBAZIAN-YASSAR R, LI Ju, HU Liang-bing. Carbothermal shock synthesis of high-entropy-alloy nanoparticles [J]. Science, 2018, 359(6383): 1489−1494.

[21] SHI Pei-jian, REN Wei-li, ZHENG Tian-xiang, REN Zhong-ming, HOU Xue-ling, PENG Jian-chao, HU Peng-fei, GAO Yan-fei, ZHONG Yun-bo, LIAW P K. Enhanced strength-ductility synergy in ultrafine-grained eutectic high-entropy alloys by inheriting microstructural lamellae [J]. Nature Communications, 2019, 10: 489.

[22] SHI Pei-jian, LI Run-guang, LI Yi, WEN Yue-bo, ZHONG Yun-bo, REN Wei-li, SHEN Zhe, ZHENG Tian-xiang, PENG Jian-chao, LIANG Xue, HU Peng-fei, MIN Na, ZHANG Yong, REN Yang, LIAW P K, RAABE D, WANG Yan-dong. Hierarchical crack buffering triples ductility in eutectic herringbone high-entropy alloys [J]. Science, 2021, 373(6557): 912−918.

[23] FAN Lei, YANG Tao, ZHAO Yi-lu, LUAN Jun-hua, ZHOU Gang, WANG Hao, JIAO Zeng-bao, LIU C T. Ultrahigh strength and ductility in newly developed materials with coherent nanolamellar architectures [J]. Nature Communications, 2020, 11: 6240.

[24] WU Qing-feng, HE Feng, LI Jun-jie, KIM H S, WANG Zhi-jun, WANG Jin-cheng. Phase-selective recrystallization makes eutectic high-entropy alloys ultra-ductile [J]. Nature Communications, 2022, 13: 4697.

[25] DU X H, LI W P, CHANG H T, YANG T, DUAN G S, WU B L, HUANG J C, CHEN F R, LIU C T, CHUANG W S, LU Y, SUI M L, HUANG E W. Dual heterogeneous structures lead to ultrahigh strength and uniform ductility in a Co−Cr−Ni medium-entropy alloy [J]. Nature Communications, 2020, 11: 2390.

[26] XIE Peng-fei, YAO Yong-gang, HUANG Zhen-nan, LIU Zhen-yu, ZHANG Jun-lei, LI Tang-yuan, WANG Guo-feng, SHAHBAZIAN-YASSAR R, HU Liang-bing, WANG Chao. Highly efficient decomposition of ammonia using high-entropy alloy catalysts [J]. Nature Communications, 2019, 10: 4011.

[27] ZHAN Chang-hong, XU Yong, BU Ling-zheng, ZHU Hua-ze, FENG Yong-gang, YANG Tang, ZHANG Ying, YANG Zhi-qing, HUANG Bo-long, SHAO Qi, HUANG Xiao-qing. Subnanometer high-entropy alloy nanowires enable remarkable hydrogen oxidation catalysis [J]. Nature Communications, 2021, 12: 6261.

[28] YANG Fu-sheng, WANG Jing, ZHANG Yang, WU Zhen, ZHANG Zao-xiao, ZHAO Feng-qi, HUOT J, GROBIVĆ N J, NOVAKOVIĆ N. Recent progress on the development of high entropy alloys (HEAs) for solid hydrogen storage: A review [J]. International Journal of Hydrogen Energy, 2022, 47(21): 11236−11249.

[29] KAO Y F, CHEN S K, SHEU J H, LIN Jiun-ting, LIN Wei-en, YEH J W, LIN Su-jien, LIOU T H, WANG C W. Hydrogen storage properties of multi-principal-component $CoFeMnTi_xV_yZr_z$ alloys [J]. International Journal of Hydrogen Energy, 2010, 35(17): 9046−9059.

[30] MA Xiang-feng, DING Xin, CHEN Rui-run, GAO Xue-feng, SU Yan-qing, CUI Hong-zhi. Enhanced hydrogen storage properties of $ZrTiVAl_{1-x}Fe_x$ high-entropy alloys by modifying the Fe content [J]. RSC Advances, 2022, 12(18): 11272−11281.

[31] LAI Da-wei, LING Li, SU Meng-fei, KANG Qiao-ling, GAO Feng, LU Qing-yi. From amorphous to crystalline: A universal strategy for structure regulation of high-entropy transition metal oxides [J]. Chemical Science, 2023, 14(7): 1787−1796.

[32] HUANG Wen-jiang, MARTIN P, ZHUANG Hou-long. Machine-learning phase prediction of high-entropy alloys [J]. Acta Materialia, 2019, 169: 225−236.

[33] KING D J M, MIDDLEBURGH S C, MCGREGOR A G, CORTIE M B. Predicting the formation and stability of single phase high-entropy alloys [J]. Acta Materialia, 2016, 104: 172−179.

[34] REED-HILL R E. Physical metallurgy principles [M]. 3nd ed. PWS-KENT, 1972.

[35] ZHANG Yong, ZHOU Yun-jun, LIN Jun-pin, CHEN Guo-liang, LIAW P K. Solid-solution phase formation rules for multi-component alloys [J]. Advanced Engineering Materials, 2008, 10(6): 534−538.

[36] MIEDEMA A R, DECHATEL P F, DEBOER F R. Cohesion in alloys-fundamentals of a semi-empipical model [J]. Physica B & C, 1980, 100(1): 1−28.

[37] FANG Shou-shi, XIAO Xue-shan, LEI Xia, LI Wei-huo, DONG Yuan-da. Relationship between the widths of supercooled liquid regions and bond parameters of Mg-based bulk metallic glasses [J]. Journal of Non-Crystalline Solids, 2003, 321(1/2): 120−125.

[38] GUO Sheng, LIU C T. Phase stability in high entropy alloys: Formation of solid-solution phase or amorphous phase [J]. Progress in Natural Science: Materials International, 2011, 21(6): 433−446.

[39] LIU C T. Physical metallurgy and mechanical properties of ductile ordered alloys $(Fe,Co,Ni)_3V$ [J]. International Metals Reviews, 2013, 29(1): 168−194.

[40] GUO Sheng, NG Chun, LU Jian, LIU C T. Effect of valence electron concentration on stability of fcc or bcc phase in high entropy alloys [J]. Journal of Applied Physics, 2011, 109(10): 103505.

[41] GAO M C, ALMAN D E. Searching for next single-phase high-entropy alloy compositions [J]. Entropy, 2013, 15: 4504−4519.

[42] JIANG L, LU Yi-ping, JIANG H, WANG T M, WEI B N, CAO Z Q, LI T J. Formation rules of single phase solid solution in high entropy alloys [J]. Materials Science and Technology, 2016, 32(6): 588−592.

[43] YANG Xiao, ZHANG Yong. Prediction of high-entropy stabilized solid-solution in multi-component alloys [J]. Materials Chemistry and Physics, 2012, 132(2): 233−238.

[44] SENKOV O N, MIRACLE D B. A new thermodynamic parameter to predict formation of solid solution or intermetallic phases in high entropy alloys [J]. Journal of Alloys and Compounds, 2016, 658: 603−607.

[45] RAGHAVAN R, HARI KUMAR K C, MURTY B S. Analysis of phase formation in multi-component alloys [J]. Journal of Alloys and Compounds, 2012, 544: 152−158.

[46] MANSOORI G A, CARNAHAN N F, STARLING K E, LELAND T W. Equilibrium thermodynamic properties of the mixture of hard spheres [J]. The Journal of Chemical Physics, 1971, 54(4): 1523−1525.

[47] SINGH A K, KUMAR N, DWIVEDI A, SUBRAMANIAM A. A geometrical parameter for the formation of disordered solid solutions in multi-component alloys [J]. Intermetallics, 2014, 53: 112−119.

[48] YIN Ke-xin, DONG Geng-yi, ZHANG Guo-jin, TIAN Quan-wei, WANG Yi-nong, HUANG J C. Prediction of phase structures of solid solutions for high entropy alloys [J]. Journal of Materials Research and Technology, 2023, 24: 7654−7665.

[49] DURODOLA J F. Machine learning for design, phase transformation and mechanical properties of alloys [J]. Progress in Materials Science, 2022, 123: 100797.

[50] TRIPATHI M K, KUMAR R, TRIPATHI R. Big-data driven approaches in materials science: A survey [J]. Materials Today: Proceedings, 2020, 26: 1245−1249.

[51] ZHANG Yan, WEN Cheng, WANG Chang-xin, ANTONOV S, XUE De-zhen, BAI Yang, SU Yan-jing. Phase prediction in high entropy alloys with a rational selection of materials descriptors and machine learning models [J]. Acta Materialia, 2020, 185: 528−539.

[52] ZHAO D Q, PAN Shao-peng, ZHANG Yong, LIAW P K, QIAO Jun-wei. Structure prediction in high-entropy alloys with machine learning [J]. Applied Physics Letters, 2021, 118(23): 231904.

[53] RAO Zi-yuan, TUNG Po-yen, XIE Rui-wen, WEI Ye, ZHANG Hong-bin, FERRARI A, KLAVER T P, KÖRMANN F, SUKUMAR P T, KWIATKOWSKI D S, CHEN Yao, LI Zhi-ming, PONGE D, NEUGEBAUER J, GUTFLEISCH O, BAUER S, RAABE D. Machine learning-enabled high-entropy alloy discovery [J]. Science, 2022, 378(6615): 78−85.

[54] GÓMEZ-BOMBARELLI R, WEI J N, DUVENAUD D, HERNáNDEZ-LOBATO J, SáNCHEZ-LENGELING B, SHEBERLA D, AGUILERA-IPARRAGUIRRE J, HIRZEL T D, ADAMS R P, ASPURU-GUZIK A. Automatic chemical design using a data-driven continuous representation of molecules [J]. ACS Central Science, 2018, 4(2): 268−276.

[55] GAO M C, YEH J W, LIAW P K, ZHANG Yong. High-entropy alloys: Fundamentals and applications [M]. 1nd ed. Springer International Publishing, 2016.

[56] LI Chuan-de, LI Jian-chen, ZHAO Ming, JIANG Qing. Effect of aluminum contents on microstructure and properties of Al_xCoCrFeNi alloys [J]. Journal of Alloys and Compounds, 2010, 504(Suppl): S515−S518.

[57] LI Bao-yu, PENG Kun, HU Ai-ping, ZHOU Ling-ping, ZHU Jia-jun, LI De-yi. Structure and properties of $FeCoNiCrCu_{0.5}Al_x$ high-entropy alloy [J]. Transactions of Nonferrous Metals Society of China, 2013, 23(3): 735−741.

[58] WU Jian, QIU Huan, ZHU He-guo, XIE Zong-han, CHENG Jia-lin. Influences of Si and C addition on microstructure and mechanical properties of $Fe_{2.5}$CoNiCu high-entropy alloy [J]. Transactions of Nonferrous Metals Society of China, 2023, 33(11): 3406−3417.

[59] YOUSSEF K M, ZADDACH A J, NIU Chang-ning, IRVING D L, KOCH C C. A novel low-density, high-hardness, high-entropy alloy with close-packed single-phase nanocrystalline structures [J]. Materials Research Letters, 2014, 3(2): 95−99.

[60] EDALATI P, MOHAMMADI A, KETABCHI M, EDALATI K. Ultrahigh hardness in nanostructured dual-phase high-entropy alloy AlCrFeCoNiNb developed by high-pressure torsion [J]. Journal of Alloys and Compounds, 2021, 884: 161101.

[61] CHEN S T, TANG W Y, KUO Yen-fu, CHEN S Y, TSAU C H, SHUN T T, YEH J W. Microstructure and properties of age-hardenable $Al_xCrFe_{1.5}MnNi_{0.5}$ alloys [J]. Materials Science and Engineering: A, 2010, 527: 5818−5825.

[62] SHUN T T, HUNG C H, LEE C F. The effects of secondary elemental Mo or Ti addition in $Al_{0.3}$CoCrFeNi high-entropy alloy on age hardening at 700 °C [J]. Journal of Alloys and Compounds, 2010, 495: 55−58.

[63] MURTY B S, YEH J W, RANGANATHAN S, BHATTACHARJEE P P. High-entropy alloys [M]. 2nd ed. Elsevier, 2019.

[64] CHEN Jian, ZHOU Xue-yang, WANG Wei-li, LIU Bing, LV Yu-kun, YANG Wei, XU Da-peng, LIU Yong. A review on fundamental of high entropy alloys with promising high–temperature properties [J]. Journal of Alloys and Compounds, 2018, 760: 15−30.

[65] SENKOV O N, WILKS G B, SCOTT J M, MIRACLE D B. Mechanical properties of $Nb_{25}Mo_{25}Ta_{25}W_{25}$ and $V_{20}Nb_{20}Mo_{20}Ta_{20}W_{20}$ refractory high entropy alloys [J]. Intermetallics, 2011, 19: 698−706.

[66] TSAI M H, WANG Chun-wen, TSAI C W, SHEN Wan-jui, YEH J W, GAN J Y, WU Wen-wei. Thermal stability and performance of NbSiTaTiZr high-entropy alloy barrier for copper metallization [J]. Journal of the Electrochemical Society, 2011, 158(11): 1161−1167.

[67] HE Hao-tian, FANG Jin-xiang, WANG Jia-xuan, SUN T, YANG Zhi-qiang, MA B, CHEN H T, WEN Ming. Carbide-reinforced $Re_{0.1}Hf_{0.25}NbTaW_{0.4}$ refractory high-entropy alloy with excellent room and elevated temperature mechanical properties [J]. International Journal of Refractory Metals and Hard Materials, 2023, 116: 106349.

[68] DE L N, WANG B, WEINBERGER C R, MATSON L E, THOMPSON G B. Elevated-temperature deformation mechanisms in Ta_2C: An experimental study [J]. Acta Materialia, 2013, 61: 3905−3913.

[69] WANG Ming-liang, LU Yi-ping, LAN Jing-gang, WANG Tong-min, ZHANG Chuan, CAO Zhi-qiang, LI Ting-ju, LIAW P K. Lightweight, ultrastrong and high thermal-stable eutectic high-entropy alloys for elevated-temperature applications [J]. Acta Materialia, 2023, 248: 118806.

[70] ZHAO Yi-lu, YANG Tao, LI Yi-ran, FAN Lei, HAN Bin, JIAO Z B, CHEN Da, LIU C T, KAI J. Superior high-temperature properties and deformation-induced planar faults in a novel $L1_2$-strengthened high-entropy alloy [J]. Acta Materialia, 2020, 188: 517−527.

[71] SATHIYAMOORTHI P, KIM H S. High-entropy alloys with heterogeneous microstructure: Processing and mechanical properties [J]. Progress in Materials Science, 2022, 123: 100709.

[72] BISWAS K, GURAO N P, MAITI T, MISHRA R S. High entropy materials: Procressing, properties, and applications [M]. Springer Nature Singapore, 2022.

[73] LI Wei-dong, XIE Di, LI Dong-yue, ZHANG Yong, GAO Yan-fei, LIAW P K. Mechanical behavior of high-entropy alloys [J]. Progress in Materials Science, 2021, 118: 100777.

[74] LIU Wei-hong, HE Jun-yuang, HUANG Hai-long, WANG Hui, LU Zhao-ping, LIU C T. Effects of Nb additions on the microstructure and mechanical property of CoCrFeNi high-entropy alloys [J]. Intermetallics, 2015, 60: 1−8.

[75] CHANDA B, DAS J. Composition dependence on the evolution of nanoeutectic in $CoCrFeNiNb_x$ ($0.45 \le x \le 0.65$) high entropy alloys [J]. Advanced Engineering Materials, 2017, 20(4): 1700908.

[76] ZHANG Lin, SONG Ruo-kang, QU Guo-xin, LU Tong. Effect of nitrogen on microstructure and mechanical properties of $CrMnFeVTi_6$ high entropy alloy [J]. Transactions of Nonferrous Metals Society of China, 2021, 31(8): 2415−2427.

[77] XU Qin, CHEN De-zhi, WANG Cong-rui, CAO Wen-chao, WANG Qi, CUI Hong-zhi, ZHANG Shu-yan, CHEN Rui-run. Effects of La on microstructure and mechanical properties of $NbMoTiVSi_{0.2}$ refractory high entropy alloys [J]. Transactions of Nonferrous Metals Society of China, 2021, 31(2): 512−520.

[78] ZHAO Chen-dong, LI Jin-shan, HE Yi-xuan, WANG Jia-xiang, WANG W Y, KOU Hong-chao, WANG Jun. Effect of strong magnetic field on the microstructure and mechanical-magnetic properties of AlCoCrFeNi high-entropy alloy [J]. Journal of Alloys and Compounds, 2020, 820: 153407.

[79] NG Chun, GUO Sheng, LUAN Jun-hua, WANG Qing, LU Jian, SHI San-qiang, LIU C T. Phase stability and tensile properties of Co-free $Al_{0.5}CrCuFeNi_2$ high-entropy alloys [J]. Journal of Alloys and Compounds, 2014, 584: 530−537.

[80] NIU Si-zhe, KOU Hong-chao, GUO Tong, ZHANG Yu, WANG Jun, LI Jin-shan. Strengthening of nanoprecipitations in an annealed $Al_{0.5}CoCrFeNi$ high entropy alloy [J]. Materials Science and Engineering A, 2016, 671: 82−86.

[81] TSAI C W, TSAI M H, YEH J W, YANG C C. Effect of temperature on mechanical properties of $Al_{0.5}CoCrCuFeNi$ wrought alloy [J]. Journal of Alloys and Compounds, 2010, 490: 160−165.

[82] CHAO Qi, JOSEPH J, ANNASAMY M, HODGSON P, BARNETT M R, FABIJANIC D. $Al_xCoCrFeNi$ high entropy alloys from metal scrap: Microstructure and mechanical properties [J]. Journal of Alloys and Compounds, 2024, 976: 173002.

[83] DAOUD H M, MANZONI A, VöLKL R, WANDERKA N, GLATZEL U. Microstructure and tensile behavior of $Al_8Co_{17}Cr_{17}Cu_8Fe_{17}Ni_{33}$ (at.%) high-entropy alloy [J]. JOM, 2013, 65(12): 1805−1814.

[84] GWALANI B, SONI V, LEE M, MANTRI S A, REN Yang, BANERJEE R. Optimizing the coupled effects of Hall−Petch and precipitation strengthening in a $Al_{0.3}CoCrFeNi$ high entropy alloy [J]. Materials & Design, 2017, 121: 254−260.

[85] WANG En-hao, LI Jia-qi, KANG Fu-wei, JIANG Feng-chun, LV Li-song, DAI Bo, CAO Yang, JIANG Wei. Balancing the mechanical properties of $Al_{0.45}CoCrFeNiTi_x$ high-entropy alloys by tailoring titanium content [J]. Journal of Materials Research and Technology, 2024, 28: 967−979.

[86] SANCHEZ J M, GALARRAGA H, DEL MOLINO E, ALBIZURI J, GURAYA T, HUDSON S W. Microstructure and mechanical properties of two novel scrap tolerant $Al_{65}Cu_{10}Mg_{10}Si_{10}Zn_5$ and $Al_{80}Cu_5Mg_5Si_5Zn_5$ high entropy aluminum alloys [J]. Intermetallics, 2023, 162: 108023.

[87] SHAFIEI A, KHANI MOGHANAKI S, AMIRJAN M. Effect of heat treatment on the microstructure and mechanical properties of a dual phase $Al_{14}Co_{41}Cr_{15}Fe_{10}Ni_{20}$ high entropy alloy [J]. Journal of Materials Research and Technology, 2023, 26: 2419−2431.

[88] GE Fei-yu, YUAN Hao-ming, GAO Qi, PENG Tao, GUO Si-yang, LYU Peng, GUAN Qing-feng, LIU Hai-xia, LIU Xin-lin, GUAN Jin-tong. Microstructure, hardness and wear resistance of $AlCoCrFeNiTa_x$ (x= 0, 0.1, 0.3) high-entropy alloys enhanced by laser remelting and Ta addition [J]. Journal of Alloys and Compounds, 2023, 949: 169741.

[89] MING Kai-sheng, BI Xiao-fang, WANG Jian. Precipitation strengthening of ductile $Cr_{15}Fe_{20}Co_{35}Ni_{20}Mo_{10}$ alloys [J]. Scripta Materialia, 2017, 137: 88−93.

[90] SHIM S H, POURALIAKBAR H, KIM Y K, LEE B J, FALLAH V, KIM Y K, LIM K R, NA Y S, HONG S I. Exploring the impact of heat treatment on the transformation of hierarchical microstructure and mechanical properties in a non-equiatomic CrMnFeNiCu high-entropy alloy with a reversible structure [J]. Journal of Alloys and Compounds, 2023, 969: 172514.

[91] BAKER I, MENG Fan-ling, WU M, BRANDENBERG A. Recrystallization of a novel two-phase FeNiMnAlCr high entropy alloy [J]. Journal of Alloys and Compounds, 2016, 656: 458−464.

[92] JIAO Hai-tao, WU Wen-sheng, HOU Zong-bo, TANG Yan-chuan, HU Yong, LIU De-jia, ZHAO Long-zhi. Microstructure and mechanical properties of $Fe_{50}Mn_{30}Co_{10}Cr_{10}$ high-entropy alloy with Si addition prepared by laser melting deposition [J]. Materials Today Communications, 2024, 38: 107694.

[93] DONG Pei-lin, HUANG Liu-fei, YANG Qiu-ju, ZHAO Xiao-jun, ZHONG Zhi-yong, LI Jin-feng. Mechanical and magnetic properties of nonequiatomic $Fe_{33}Co_{28}Ni_{28}Ta_5Al_6$ high entropy alloy by laser melting deposition [J]. Vacuum, 2024, 220: 112854.

[94] XIAO Ya-ke, PENG Xiang-he. Design of lightweight $Ti_3Zr_{1.5}NbV_x$ refractory high-entropy alloys with superior mechanical properties [J]. Journal of Materials Research and Technology, 2023, 27: 330−341.

[95] SHI Jie, ZHANG Yan-zhi, WANG Xun-li, JIANG Chun-li, WANG Meng, MA Ce, HUANG He. Microstructure and mechanical properties of $UNbTiHf_{1-x}Mo_x$ high-entropy alloys [J]. Materials Science and Engineering A, 2022, 860: 144239.

[96] HUDA Z. Strengthening mechanisms in metals/alloys [M].

Springer International Publishing, 2022.

[97] ZHANG Wei, MA Zhi-chao, ZHAO Hong-wei, REN Lu-quan. Refinement strengthening, second phase strengthening and spinodal microstructure-induced strength-ductility trade-off in a high-entropy alloy [J]. Materials Science and Engineering A, 2022, 847: 143343.

[98] OTTO F, DLOUHý A, SOMSEN C, BEI H, EGGELER G, GEORGE E P. The influences of temperature and microstructure on the tensile properties of a CoCrFeMnNi high-entropy alloy [J]. Acta Materialia, 2013, 61: 5743−5755.

[99] YANG Dan-ni, LIU Yong, JIANG Hao-peng, LIAO Ming-qing, QU Nan, HAN Tian-yi, LAI Zhong-hong, ZHU Jing-chuan. A novel FeCrNiAlTi-based high entropy alloy strengthened by refined grains [J]. Journal of Alloys and Compounds, 2020, 823: 153729.

[100] GIGAX J G, EL-ATWANI O, MCCULLOCH Q, AYTUNA B, EFE M, FENSIN S, MALOY A, LI Nan. Micro-and mesoscale mechanical properties of an ultra-fine grained CrFeMnNi high entropy alloy produced by large strain machining [J]. Scripta Materialia, 2020, 178: 508−512.

[101] ASGHARI-RAD P, SATHIYAMOORTHI P, BAE J W, MOON J, PARK J M, ZARGARAN A, KIM H S. Effect of grain size on the tensile behavior of $V_{10}Cr_{15}Mn_5Fe_{35}Co_{10}Ni_{25}$ high entropy alloy [J]. Materials Science and Engineering A, 2019, 744: 610−617.

[102] QU Wei, JI Cheng, MIN Ling-lei, LIU Yu-bao, LI Wei, XING Lei, REN Hui-ping. Super capacity of boron on the grain refinement of FeCoCrNiMn high entropy alloy [J]. Journal of Alloys and Compounds, 2023, 945: 169320.

[103] SEOL J B, BAE J W, LI Zhi-ming, CHAN HAN J, KIM J G, RAABE D, KIM H S. Boron doped ultrastrong and ductile high-entropy alloys [J]. Acta Materialia, 2018, 151: 366−376.

[104] LEI Zhi-feng, LIU Xiong-jun, WU Yuan, WANG Hui, JIANG Sui-he, WANG Shu-dao, HUI Xi-dong, WU Yi-dong, GAULT B, KONTIS P, RAABE D, GU Lin, ZHANG Qing-hua, CHEN Hou-wen, WANG Hong-tao, LIU Jia-bin, AN Ke, ZENG Qiao-shi, NIEH T G, LU Zhao-ping. Enhanced strength and ductility in a high-entropy alloy via ordered oxygen complexes [J]. Nature, 2018, 563(7732): 546−550.

[105] WANG Zhang-wei, BAKER I, CAI Zhong-hou, CHEN Si, POPLAWSKY J D, GUO Wei. The effect of interstitial carbon on the mechanical properties and dislocation substructure evolution in $Fe_{40.4}Ni_{11.3}Mn_{34.8}Al_{7.5}Cr_6$ high entropy alloys [J]. Acta Materialia, 2016, 120: 228−239.

[106] HU Yue-feng, GAN Ke-fu, ZHANG Yong, YAN Ding-shun, YANG Qian-kun, ZHU Shu-ya, LI Zhi-ming. Dual-interstitials promoted multiple mechanisms enhance strength-ductility synergy of an equiatomic high-entropy alloy [J]. Journal of Alloys and Compounds, 2023, 968: 172271.

[107] LIU Li-yuan, ZHANG Yang, HAN Ji-hong, WANG Xi-yu, JIANG Wen-qing, LIU C T, ZHANG Zhong-wu, LIAW P K. Nanoprecipitate-strengthened high-entropy alloys [J]. Advanced Science, 2021, 8: 2100870.

[108] HE Jun-yang, WANG Hui, HUANG Hai-long, XU Xian-dong, CHEN Ming-wei, WU Yuan, LIU Xing-jiang, NIEH T G, AN Ke, LU Zhao-ping. A precipitation-hardened high-entropy alloy with outstanding tensile properties [J]. Acta Materialia, 2016, 102: 187−196.

[109] WANG Zhao-guang, ZHOU Wei, FU Li-ming, WANG Jun-feng, LUO Rui-chun, HAN Xiao-cang, CHEN Bin, WANG Xiao-dong. Effect of coherent $L1_2$ nanoprecipitates on the tensile behavior of a fcc-based high-entropy alloy [J]. Materials Science and Engineering A, 2017, 696: 503−510.

[110] SINGH S, WANDERKA N, MURTY B S, GLATZEL U, BANHART J. Decomposition in multi-component AlCoCrCuFeNi high-entropy alloy [J]. Acta Materialia, 2011, 59: 182−190.

[111] TSAI M H, YUAN Hao, CHENG Guang-ming, XU Wei-zong, TSAI K Y, TSAI C W, JIAN W W, JUAN C C, SHEN Wan-Jui, CHUANG Ming-Hao, YEH J W, ZHU Y T. Morphology, structure and composition of precipitates in $Al_{0.3}CoCrCu_{0.5}FeNi$ high-entropy alloy [J]. Intermetallics, 2013, 32: 329−336.

[112] JANG T J, CHOI W S, KIM D W, CHOI G, JUN H, FERRARI A, KöRMANN F, CHOI P P, SOHN S S. Shear band-driven precipitate dispersion for ultrastrong ductile medium-entropy alloys [J]. Nature Communications, 2021, 12: 4703.

[113] LIU Li-yuan, ZHANG Yang, LI Jun-peng, FAN Ming-yu, WANG Xi-yu, WU Guang-chuan, YANG Zhong-bo, LUAN Jun-hua, JIAO Zeng-bao, LIU C T, LIAW P K, ZHANG Zhong-wu. Enhanced strength-ductility synergy via novel bifunctional nano-precipitates in a high-entropy alloy [J]. International Journal of Plasticity, 2022, 153: 103235.

[114] KAMINSKII A A, AKCHURIN M S, GAINUTDINOV R V, TAKAICHI K, SHIRAKAVA A, YAGI H, YANAGITANI T, UEDA K. Microhardness and fracture toughness of Y_2O_3- and $Y_3Al_5O_{12}$-based nanocrystalline laser ceramics [J]. Crystallography Reports, 2005, 50(5): 869−873.

[115] GWALANI B, POHAN R M, LEE J, LEE B, BANERJEE R, RYU H J, HONG S H. High-entropy alloy strengthened by in situ formation of entropy-stabilized nano-dispersoids [J]. Scientific Reports, 2018, 8(1): 14085.

[116] CHENG Zhuo, YANG Lu, MAO Wen-hao, HUANG Zhi-kun, LIANG Ding-shan, HE Bin, REN Fu-zeng. Achieving high strength and high ductility in a high-entropy alloy by a combination of a heterogeneous grain structure and oxide-dispersion strengthening [J]. Materials Science and Engineering A, 2021, 805: 140544.

[117] GROSDIDIER T, JI Gang, LAUNOIS S. Processing dense hetero-nanostructured metallic materials by spark plasma sintering [J]. Scripta Materialia, 2007, 57: 525−528.

[118] MORAVCIK I, GOUVEA L, HORNIK V, KOVACOVA Z, KITZMANTEL M, NEUBAUER E, DLOUHY I. Synergic strengthening by oxide and coherent precipitate dispersions in high-entropy alloy prepared by powder metallurgy [J]. Scripta Materialia, 2018, 157: 24−29.

[119] ZHANG Rui-zhi, REECE M J. Review of high entropy ceramics: Design, synthesis, structure and propertie [J]. Journal of Materials Chemistry A, 2019,7: 22148−22162.

[120] CHEN Shuai, AITKEN Z H, PATTAMATTA S, WU Zhao-xuan, YU Zhi-gen, SROLOVITZ D J, LIAW P K, ZHANG Yong-wei. Simultaneously enhancing the ultimate strength and ductility of high-entropy alloys via short-range ordering [J]. Nature Communications, 2021, 12: 4953.

[121] JI Wei-ming, WU Mao-see. Retainable short-range order

effects on the strength and toughness of NbMoTaW refractory high-entropy alloys [J]. Intermetallics, 2022, 150: 107707.
[122] GAO Xue-feng, CHEN Rui-run, LIU Tong, FANG Hong-ze, QIN Gang, SU Yan-qing, GUO Jing-jie. High-entropy alloys: A review of mechanical properties and deformation mechanisms at cryogenic temperatures [J]. Journal of Materials Science, 2022, 57: 1−34.
[123] HERRERA C, PONGE D, RAABE D. Design of a novel Mn-based 1GPa duplex stainless TRIP steel with 60% ductility by a reduction of austenite stability [J]. Acta Materialia, 2011, 59: 4653−4664.
[124] CHEN Si-jing, OH H S, GLUDOVATZ B, KIM S J, PARK E S, ZHANG Ze, RITCHIE R O, YU Qian. Real-time observations of TRIP-induced ultrahigh strain hardening in a dual-phase CrMnFeCoNi high-entropy alloy [J]. Nature Communications, 2020, 11: 826.
[125] WU Xiao-xiang, MAYWEG D, PONGE D, LI Zhi-ming. Microstructure and deformation behavior of two TWIP/TRIP high entropy alloys upon grain refinement [J]. Materials Science and Engineering A, 2021, 802: 140661.
[126] ELETI R R, KLIMOVA M, TIKHONOVSKY M, STEPANOV N, ZHEREBTSOV S. Exceptionally high strain-hardening and ductility due to transformation induced plasticity effect in Ti-rich high-entropy alloys [J]. Scientific Reports, 2020, 10(1): 13293.
[127] WANG Lu, FU Chao, WU Yi-dong, LI Run-guang, HUI Xi-dong, WANG Yan-dong. Superelastic effect in Ti-rich high entropy alloys via stress-induced martensitic transformation [J]. Scripta Materialia, 2019, 162: 112−117.
[128] WANG Lu, FU Chao, WU Yi-dong, LI Run-guang, WANG Yan-dong, HUI Xi-dong. Ductile Ti-rich high-entropy alloy controlled by stress induced martensitic transformation and mechanical twinning [J]. Materials Science and Engineering A, 2019, 763: 138147.
[129] YANG Lu, LIANG Ding-shan, CHENG Zhuo, DUAN Ran-xi, ZHONG Chuan-xin, LUAN Jun-hua, JIAO Zeng-bao, REN Fu-zeng. Simultaneous enhancement of strength and ductility via microband formation and nanotwinning in an $L1_2$-strengthened alloy [J]. Fundamental Research, 2022, 7: 12.
[130] HUANG A, ZHANG Cheng, LI Ze-zhou, WANG Hao-ren, XU Ming-jie, ZHU Chao-yi, WANG Xin, MEYERS M A, LAVERNIA E J. Dynamic mechanical performance of FeNiCoAl-based high-entropy alloy: Enhancement via microbands and martensitic transformation [J]. Materials Today Advances, 2023, 20: 100439.
[131] GUTIERREZ-URRUTIA I, RAABE D. Microbanding mechanism in an Fe−Mn−C high-Mn twinning-induced plasticity steel [J]. Scripta Materialia, 2013, 69: 53−56.
[132] KELLER R, ZIELINSKI W, GERBERICH W W. On the onset of low-energy dislocation substructures in fatigue: Grain size effects [J]. Materials Science and Engineering A, 1989, 113: 267−280.

高熵合金的相形成预测和力学响应

李 彬[1]，孙加林[1,2,3]，赵 军[4]，运侠伦[5]，杜全斌[6]

1. 山东大学 机电与信息工程学院，威海 264209；
2. 山东大学深圳研究院，深圳 518057；
3. 中国科学院 兰州化学物理研究所 固体润滑国家重点实验室，兰州 730000；
4. 山东大学 机械工程学院 高效洁净机械制造教育部重点实验室，济南 250061；
5. 西安交通大学 机械工程学院 机械制造系统工程国家重点实验室，西安 710049；
6. 河南机电职业学院 河南省超硬材料智能制造装备集成重点实验室，郑州 451191

摘 要：高熵合金是通过混合多种主成分引入化学无序而获得的新型材料，具有显著优于传统合金的结构和性能。然而，强度和塑性的不协调关系在高熵合金系统中依然存在，严重限制了高熵合金的实际应用。此外，采用试错法制备高熵合金耗时费力，浪费资源，阻碍了高熵合金的高速高质量发展。综述了高熵合金的最新进展，阐明了预测相结构形成的方法和影响力学性能的关键因素。此外，重点分析了高熵合金的强韧化策略，从而进一步扩展其应用领域。最后，提出了高熵合金面临的挑战和未来的研究方向。

关键词：高熵合金；相结构预测；力学响应；强韧化策略；密度泛函理论

(Edited by Bing YANG)